Laboratory analysis of volcanic ash particles using a 2D video disdrometer

Sung-Ho Suh[1], Masayuki Maki[2*], Masato Iguchi[3], Dong-In Lee[1],

Tatsuya Momotani[4], and Akihiko Yamaji[4]

Institutional addresses:

[1]Department of Environmental Atmospheric Sciences, Pukyong National University, Namgu, Busan, Republic of Korea

[2]Research and Education Center for Natural Hazards, Kagoshima University, Korimoto, Kagoshima, Japan

[3]Sakurajima Volcano Research Center, Disaster Prevention Research Institute, Kyoto University, Sakurajima, Kagoshima, Japan

[4]Japan Weather Association, Higashi-Ikebukuro, Toshima-ku, Tokyo, Japan

* Corresponding author: Masayuki Maki, (maki@gm.kagoshima-u.ac.jp)

Key Points: Volcanic ash, 2DVD, aerodynamic properties, laboratory experiments

21   The English in this document has been checked by at least two professional editors, both native
22   speakers of English. For a certificate, please see:

24   http://www.textcheck.com/certificate/7pU3Ux

Abstract

Radar variables of volcanic ash clouds are dependent on microphysical processes and can be expressed using physical parameters of volcanic ash particles, such as terminal velocity, axis ratio, and canting angle, which are necessary for quantitative ash-fall estimations. In this study, free-fall experiments of volcanic ash were accomplished using a two-dimensional video disdrometer under controlled conditions.

Samples containing a rotating symmetric axis were selected and divided into five types according to shape and orientation, i.e., oblate and prolate spheroids with horizontally and vertically oriented axes and spheres. The horizontally and vertically oriented particles were present in proportions of 75.5% and 21.6%, and oblate and prolate spheroids were in proportions of 76.2% and 23.8%, respectively. The most common shape type was a horizontally oriented oblate spheroid (57.3%).

The terminal velocities were classified according to shape type. The terminal velocities of prolate spheroids (vertically oriented) particles were higher than those of oblate spheroids (horizontally). Terminal velocities were in the range $0.5 <$ volume–equivalent spherical particle diameter (D) < 1 mm for OH because of an increase in axis ratio and a sharp decrease in sample size from $D < 0.7$ mm. The axis ratios fell over a wide range, from 0 to 1.5, at $D < 2$ mm, but converged to 0.94 at $D > 2$ mm.

The histogram of canting angles followed unimodal and bimodal distributions with respect to horizontally and vertically oriented particles, respectively. The mean values were close to $0°$ and the standard deviation for the entire particle shape types was close to that of raindrops ($10°$) under calm atmospheric conditions.

1. Introduction

Volcanic eruptions are considered one of the most severe types of natural disasters, and can lead to human casualties and property damage (Wilson et al., 2012; Hillman et al., 2012; Sigurdsson et al., 2015; Wilson et al., 2015). Following an eruption, fine airborne volcanic ash flows for several tens of kilometers, which can cause major problems by increasing aviation traffic (e.g., Bonadonna et al., 2012; Langmann et al., 2012); this was seen after the eruption of Eyjafjallajökull volcano in Iceland during the period April 14– 21, 2010, for example (Bonadonna et al., 2011). From the viewpoint of volcanological hazard reduction, trajectory modeling of volcanic ash clouds is an important research topic. The aim of numerical forecasting modeling is to accurately predict the transport and deposition of ash, which is vitally important for hazard mitigation (Poulidis et al., 2017). Current numerical simulations consider the terminal velocity (V_T) of particles and incorporate wind advection, atmospheric diffusion, and particle aggregation (Folch, 2012; Bonadonna et al., 2015). The V_T of a particle is affected by its shape, density particle volume fraction, and atmospheric properties, such as air pressure (P), temperature (T), and vertical flow (Wilson and Huang, 1979; Haider and Levenspiel, 1989; Ganser, 1993; Bonadonna et al., 1998; Riley, 2003; Dellino, 2005; Coltelli et al., 2008; Alfano et al., 2011; Del Bello et al., 2017). Observational analysis would be helpful for improving the performance of eruption models; however, there is limited information on the microphysical characteristics and inner structures of volcanic ash clouds (Marzano et al., 2006; 2012). Transport and sedimentation of volcanic ash are complex processes, and the residence time and fall velocity of ash is critically dependent on particle size (Bonadonna et al., 1998), where with respect to the latter, smaller particles could be flowing in the atmosphere further from the vent. Ash consists of very fine-grained fragments, volume-equivalent spherical particle diameter (D in mm) is generally smaller than 2 mm, and these are generally dominated by broken glass shards rather than crystal and lithic fragments. Bombs, resulting from larger eruptions, may show vesicularity; they exhibit flexibility similar to

72 plastic when a volcano becomes active and erupts (Sparks et al., 1997; Marzano et al., 2006; 2012).

73 The trajectories of volcanic ash clouds can be detected by meteorological satellites (Stevenson et al.,

74 2015), and the ash amounts can be observed using a ground-based paper cup and an electronic balance

75 (Tajima et al., 2015, Maki et al., 2016). Covering the middle latitudes of the entire globe, geostationary

76 meteorological satellites are able to detect water clouds over the ocean, even when they are far from

77 land; they are also more capable of detecting the upper layers of weather systems, such as convective

78 cells and typhoons, than other weather observational instruments, albeit with relatively low spatial

79 resolution (a few kilometers). When operating in near-polar orbiting mode, these sensors have higher

80 spatial resolution but are limited by their lower temporal resolution, and only pass over a given area

81 twice per day. Weather radar operates for a similar purpose to that of meteorological satellites, and

82 provides information for determining the volume, mass, and echo top height of weather systems. Short-

83 duration eruptions, i.e., less than 1 hour, can be detected at high spatio-temporal resolution, especially

84 in the early period of an eruption. The temporal resolution of weather radar is a few minutes for a

85 single volume scan, and depends on the observation strategy and radar band. The spatial resolution of

86 weather radar is a few hundred meters and is proportional to the radar frequency. A number of ash

87 cloud detections were reported in several observational cases in the US and Japan (Maki and Doviac,

88 2001; Maki et al., 2012). Marzano et al. (2013) summarized 28 major explosive volcanic eruptions

89 detected by weather radars from 1970 to 2011.

90   Harris and Rose (1983) attempted to analyze volcanic ash particle size and total mass using a C-

91 band weather radar. Maki and Doviac (2001) found that a weather radar could measure the radar

92 reflectivity factor (z in mm^6 m^{-3}) of volcanic ash columns and Donnadieu et al. (2012) detected

93 volcanic eruptions using an L-band fixed radar. Marzono et al. (2006, 2012) and Maki et al. (2012,

94 2014) detected and analyzed volcanic eruptions using weather radars, from theoretical (physical) and

95 experimental (engineering) perspectives. These weather radars were developed to detect hydrometeors

96 with a size range from millimeters to centimeters. Coarse particles (D < 0.53 mm) can be detected by

97 weather radars. Coarse volcanic ash particles are deposited rapidly following an eruption within a few

98 tens of kilometers from the vent (Bonadonna et al., 1998; Beckett et al., 2015); however, smaller

99 particles, such as fine ash (D < 64 μm), are transported over distances of several thousands of

100 kilometers and cannot be detected by operational weather radar, since the minimum detectable

101 reflectivity (MDR) of radar is inversely proportional to the distance between the radar and the target,

102 and where this depends on the wavelength of the transmitted wave (Sauvageot, 1992; Maki et al., 2016).

103   Weather radars require detailed information on the following basic parameters: particle size

104 distribution (PSD), particle density (ρ_s in g cm^{-3}), dielectric constant ($|K|^2$), V_T (in m s^{-1}), axis ratio (γ),

105 and canting angle (β in °) to estimate ash amount quantitatively, and these can all be observed by a

106 ground-based instrument. The PSD is controlled by the microphysical processes of the volcanic

107 eruption system and plays an important role in its development; it is also essential for accurate

108 evaluation of the backscattering and absorption of particles (Seliga and Bringi, 1976; Marzano et al.,

109 2006; 2012), which affect the radar variables. There are two basic PSD models: i) the gamma size

110 distribution following the gamma function (Γ) and ii) the Weibull size distribution, mainly applied as

111 a log-normal PSD. The former is as a well-known reference in radar meteorology. For precipitation,

112 several raindrop size distribution (DSD) models can be used in a variety of cases (e.g., Ulbrich, 1983;

113 Testud et al., 2001). This implies that a disdrometer is necessary to analyze the observed radar variables

114 and evaluate them in a scattering simulation.

115   The ashfall rate (R_A) can be also defined in terms of the V_T and is determined by ρ_s, shape, and

116 orientation (Ganser, 1993; Hölzer and Martin Sommerfeld, 2008; Mandø and Rosendahl. 2010;

117 Bagheri and Bonadonna, 2016; Dioguardi et al., 2017). The V_T of particles vary widely due to their

118 irregular shapes and material components (e.g., Wilson, 1972; Harris and Rose, 1983; Bonadonna et

119 al., 2011, Maki et al., 2016)

120   Volcanic ash particles have a range of shapes, and this presents a major challenge when analyzing

121   their characteristics. To address this, Böhm (1989) analyzed the aerodynamic properties of an irregular

122   hydrometeor and Huang (2010, 2015) applied this concept to snow particles. Recently, the irregularity

123   of volcanic ash particles was analyzed in detail based on the features of various regular particles, such

124   as cubes, cylinders, and disks (Bagheri and Bonadonna, 2016), using a computed tomography (CT)

125   scanner (Dioguardi et al., 2017; Garboczi et al., 2017).

126   The particle shape observed by radar depends on oscillation or tumbling and can be expressed

127   quantitatively using the β. Research on the β of volcanic ash based on meteorological radar is scarce.

128   Marzano et al. (2012) assumed that the standard deviations of the canting angle (σ_β) were 30° and 10°

129   under unstable conditions (in which the tumbling phenomenon may occur) and stable conditions,

130   respectively. For the case of raindrops, the mean value of the canting angle ($\bar{\beta}$) is close to 0° and σ_β

131   ranged from 4° to 10° (Beard and Jameson, 1983; Hendry et al., 1987; Huang et al., 2008; Ryzhkov et

132   al., 2011). Solid hydrometeors, such as snowflakes and hail, exhibited different features compared to

133   the liquid phase. The σ_β values for graupel, rimed particles, and aggregations were 20°, 16°, and 13°,

134   respectively (Garrett, 2015). Hail that occurs in the context of the tumbling phenomenon is described

135   by $\bar{\beta} = 60(1-f_w)$, where f_w is the wetting ratio (Synder et al., 2013; Jung et al., 2008). It is assumed

136   that the existence of a liquid phase water covering on the particles reduces the tumbling/oscillations

137   phenomenon.

138   The $|K|^2$ of the particle depends on the chemical components and phase. Water and ice

139   hydrometeors have quite different values of $|K|^2$, of 0.93 and 0.19, respectively, where the value

140   depends on the radar frequency and T. Volcanic ash has a silicate content proportional to the $|K|^2$,

141   resulting in various values of $|K|^2$, such as 0.34 and 0.39 ± 0.02 (Adam et al., 1996; Marzano et al.,

142   2006; Oguchi et al., 2009).

Aerodynamic properties are important for safe aviation, and for studying the effects of volcanic ash on climate change, since these parameters determine the residence time of ash particles in the atmosphere (e.g., Folch et al., 2009). There are two approaches to studying these aerodynamic properties. The first approach is physical, where a numerical simulation model is used to calculate terminal velocities, drag force, and Reynolds number (Re); examples of this approach can be found in Happel and Brenner (1983). Scattering simulations of particles may be aided by the results of the present study, allowing accurate detection of ash fall by weather radar; this could help verify observed radar variables. In particular, the T-matrix scattering simulation developed by Waterman (1965, 1971) is useful for calculation of the theoretical backscattering power of non-spherical particles. The second approach is related to engineering research, in which the aforementioned relationships are determined experimentally; examples of this approach can be found in Dellino et al. (2005), Bagheri et al. (2013), Bagheri and Bonadonna (2016), and Dioguardi et al. (2018). Particle dispersion depends on atmospheric conditions, such as T and wind, which can affect the retrieval of basic parameters. It is suggested that these parameters be analyzed through free-fall laboratory experiments, to reduce unknown information and obtain reliable results.

The present study focuses on the second approach, and its purpose is to analyze the physical parameters of volcanic ash particles statistically using a ground-based disdrometer, and to develop quantitative ash-fall estimation (QAE) methods for accurate detection of volcanic ash clouds by weather radar. The rest of this paper is organized as follows. Section 2 introduces the free-fall experiment for samples collected with a ground-based disdrometer and the classification method for particle shapes. Section 3 presents the V_T, γ and β results for each type of volcanic ash particle shape. Section 4 summarizes the results.

2. Data and Methods

a. Two dimensional (2D) video disdrometer

The 2D video disdrometer (2DVD) was developed by Joanneum Research (Graz, Austria) to detect single raindrop particles, and the instrument has been modified to cover the errors caused by turbulence effects (Nešpor et al., 2000). The device is able to observe the shape, V_T, and β of a single particle using optical light. The ability to analyze a single particle is a significant advantage compared to other disdrometers, such as the Joss-Waldvogel disdrometer (JWD), the Precipitation Occurrence Sensor System (POSS), and Parsivel (PARticle Size and VELocity). For instance, Parsivel considers a fixed measurement area without any consideration of particle shape (e.g., Tokay et al., 2014), while 2DVD observes particles by passing them through a 100 cm^2 observation area consisting of two light sources and reflecting mirrors and two cameras, one set 6.2 mm above the other, and collects data with a resolution of 630 pixels; this results in a pixel size of 0.2 mm at 55 kHz (Kruger and Krajewski, 2002). Particles passing through the observation area yield shape information according to the radiation intensity of the light sources, which is helpful for calculation of γ and β. The V_T of particles is calculated using the height difference between the two cameras. Based on these advantages, the oscillation and particle shape of raindrops can be analyzed by 2DVD (Thurai and Bringi, 2005; Thurai et al., 2007). Huang et al. (2010, 2015) used 2DVD to analyze the features of irregularly shaped snow. There have been few previous aerodynamic analyses of volcanic ash particles performed using 2DVD, which is able to detect and analyze volcanic ash particles with a range of irregular shapes. Thus, 2DVD offers a unique approach as a new observation strategy.

b. Definition of particle shape type

190   Volcanic ash particles have various shapes that can be detected by 2DVD (Fig. 1). In the case of

191   raindrops, the DSD is dependent upon the break-up and coalescence processes occurring via up and

192   downdrafts, since the forces of gravity and buoyancy can easily affect raindrop shapes (Rosenfeld and

193   Ulbrich, 2003). Solid particles do not readily change shape when falling without the influence of forces

194   such as collision. It is thus inferred that many particle shapes would be found in the atmosphere, and

195   that it would be possible to define and classify each particle shape type if we were able to accurately

196   detect a single particle. Thus, the range of γ for solid particles would be expected to be wide compared

197   to that of raindrops, and various values of V_T and β would likely be observed. The γ_x of a particle is

198   defined as the ratio of height to width for the observation direction x, and its representative value is

199   calculated using the geometric means of the two γ (γ_1, γ_2) detected by cameras 1 and 2, respectively

200   (Eq. 1):

201

202 $$\gamma_{1(2)} = \frac{\text{Height}_{1(2)}}{\text{Width}_{1(2)}}, \qquad \gamma = \sqrt{\gamma_1 \gamma_2}$$

203

204   Eq. (1).

205

206   The β is defined as the difference in angle between the rotating symmetric axis and vertical axis.

207   The counter-clockwise (clockwise) movement of the rotating symmetric axis has a positive (negative)

208   value and the entire range is 180° (from -90° to 90°) with 0° as the center.

209   It is necessary to consider the true axis ratio (γ_T) to correctly define the particle shape (Fig. 2). The

210   apparent axis ratio (γ_A) considers the effect of β but the γ_T does not. The 2D coordinates (x, z) of the

211   particle shape with β are defined as follows:

212

213
$$x_A = r\ \cos(\theta + \beta), \qquad z_A = r\ \sin(\theta + \beta)$$

214

215
$$x_T = r\ \cos\theta, \qquad z_T = r\ \sin\theta$$

216

217   where subscript A is the coordinate of the original data coordinate considering the β and subscript

218   T is the modified data coordinate. The symbol r refers to the length from the data point to the center

219   and the symbol θ represents the degrees of data coordinates from the positive x axis, which range

220   between 0° and 180°. In this paper, γ stands for γ_A for convenience.

221   An objective criterion for particle shape type was considered since particle shapes can be highly

222   diverse and irregular (e.g., Bagheri and Bonadonna, 2016, Dioguardi et al., 2017; Garboczi et al., 2017,

223   Dioguardi et al., 2018). In the case of irregular particles, the γ can change according to the observation

224   direction; however, any criterion should be able to define the particle shape types strictly and reliably.

225   To solve this problem, particles with a rotating symmetric axis were the main target of the present

226   study. Therefore, we considered oblate spheroid (O), prolate spheroid (P), and sphere (Sp), which all

227   have a rotating symmetric axes. Among these particle types, the major axes of the oblate and prolate

228   spheroids could be horizontally (H) and vertically (V) oriented with respect to the ground, respectively.

229   Thus, the various particle shapes were divided into five types as follows; OH, OV, PH, PV, and Sp.

230   To define these particle shape types, a strict definition of the γ_T is required, which can be calculated

231   from the β. As with the γ, the two β values are automatically calculated by 2DVD. In the case where

232   the β is assumed as 0°, the rotating symmetric axis for OH and PV can be defined, since it is observed

233   for any observation direction parallel to the ground. However, in the case of OV and PH particles, the

234   rotating symmetric axis cannot be defined when the observation direction is parallel. In the case where

235   the β is not 0°, γ_T for all particle shape types would not change when oscillation occurs in a direction

236   orthogonal to the observation direction, but it is difficult to estimate both γ_T and β when particle

237   oscillation appears in a direction parallel to the observation direction. The ability to restore the γ_T and

238   β relative to this observation direction is limited, which is one of the main disadvantages of the 2D

239   observation strategy.

240   Based on these facts, a major β was selected based on the following reasoning: i) a β for the

241   observation direction with lower (higher) γ_T for OH (PV) is selected. ii) in the case of OV (PH), for

242   which the rotating symmetric axis was observed for only one observation direction, β was considered

243   where the value of β had a higher (lower) γ_T than that of the other observation direction. Therefore, β

244   with a lower (higher) γ_T in two observation directions for the case of an oblate (prolate) particle was

245   considered as a meaningful value. The Sp could not have their value of β determined theoretically,

246   because there is the possibility of a rotating symmetric axis in any direction.

247   After removing β, each particle shape was defined using γ_T (Table 1). Note that a 10% bias range

248   was allowed, to take observational error into account. For example, a particle was considered as a

249   sphere when $0.9 < \gamma_T < 1.1$, which is an applied 10% bias range from $\gamma_T = 1$. In addition, the particle

250   types OH and PV (OV and PH) were classified when the value of $|\gamma_1 - \gamma_2|$ was smaller (larger) than

251     $0.1\gamma_T$, to consider particles with only a rotating symmetric axis.

252

253

254   **c. Calculate the terminal velocity for the various particle shape types**

255   The V_T of volcanic ash is required to estimate the R_A (kg m^{-2} s^{-1}) on the ground where this depends

256   on atmospheric density (ρ_g in g cm^{-3}), T, Re, drag coefficient (C_D), D, shape, and ρ_s. Kunii and

257   Levenspiel (1969) developed a theoretical V_T equation:

258

259
$$V_T = \left(\frac{4(\rho_s - \rho_g)gD}{3\rho_g C_D}\right)^{0.5} \qquad (10^0 < Re < 10^4)$$

260   Eq. (2)

261

262   Later, Suzuki (1983) developed a theoretical V_T equation for tephra. Bonadonna et al. (2011) then

263   modified the theoretical V_T equation suggested by Kunii and Levenspiel (1969) with observed ash data,

264   which implied that the result of the theoretical V_T equation could be unsuitable for non-spherical

265   particles. Based on these equations, various C_D equations considering non-spherical particles were

266   subsequently developed. Tran-Cong et al. (2004) developed a new equation for C_D using the function

267   of circularity and Hölzer and Somerfeld (2008) introduced a progressed C_D equation considering two

268   types of sphericity: lengthwise ($\Phi_\parallel$) and crosswise ($\Phi_\perp$). This equation is as follows:

269

270
$$C_D = \frac{8}{Re}\frac{1}{\sqrt{\Phi_\parallel}} + \frac{16}{Re}\frac{1}{\sqrt{\Phi}} + \frac{3}{\sqrt{Re}}\frac{1}{\Phi^{3/4}} + 0.42 \times 10^{0.41(-\log(\Phi))^{0.2}}\frac{1}{\Phi_\perp}$$

271   Eq. (3)

272

273   The Re is defined as:

274

275
$$Re = \frac{\rho_g V_T D}{\mu}$$

276   Eq. (4)

277

278   where μ is the dynamic viscosity (kg m^{-1} s^{-1}), which we assumed to be 1.983×10^{-5} based on

279   atmospheric conditions at a T of 25 °C. Three types of sphericity were defined as follows:

280

281
$$\Phi = \frac{\pi D^2}{SA}$$

 Eq. (5)

283

284   where SA is the surface area of the particle (mm^2). The lengthwise sphericity is defined as the ratio

285   between the cross-sectional area of the volume-equivalent sphere and the difference between half the

286   surface area and the mean of the projected vertical cross-sectional area (A_V) of the particle (Eq. 6):

287

288
$$\Phi_{\parallel} = \frac{\pi D^2}{4(0.5 \times SA - A_V)}$$

289   Eq. (6)

290

291   The crosswise sphericity is the same as the lengthwise sphericity, except for the denominator,

292   which includes the projected horizontal cross-sectional area of the particle (A_H), defined as follows:

293

294
$$\Phi_{\perp} = \frac{\pi D^2}{4 A_H}$$

295   Eq. (7)

296

297   It is noteworthy that the V_T is required to calculate the Re and V_T, which refers to the final product.

298   To solve this problem, the theoretical V_T (Eq. 2) was used as the input value of Eq. 4 until Eq. 2

299   converged.

300

301

302   **d. Sakurajima volcano**

303   Japan has around 10% (110) of all of the active volcanos in the world. Sakurajima (1,117m, 31.58º

304   N, 130.65º E, Kyushu, Japan) is an active volcanic island formed around 13,000 years ago, and its

305 tephra is approximately 57–66 % S$_i$O$_2$ Peléan-type. The major eruptions periods of Sakurajima were

306 1471–1476 (Bunmei era), 1779–1782 (An-ei era) and 1914 (Taisho era). The Japan Meteorological

307 Agency (JMA) reported that the eruption frequency of Sakurajima would increase significantly from

308 2009 (Maki et al., 2014) and the accumulated ash fall exceeded 3.5 kg m^{-2} in Kagoshima city in 2012

309 (Maki et al., 2016). The Ministry of Land, Infrastructure, Transport, and Tourism (MLITT) installed

310 an operational X-band radar 10.7 km from the vent, as well as 16 automatic volcanic ash weight

311 measurements, to observe volcanic eruptions in 2011 (Fig. 3).

312

313

e. Data collection and reanalysis

315 The data were collected by automatic volcanic ash weight measurements performed on the

316 Sakurajima volcano (Tajima et al., 2015; Maki et al., 2014; 2016). The free-fall experiments were

317 divided into two types; one was performed for each phi scale ($\Phi = -\log_2 D$) from $\Phi = 3$ to -4 (0.125 <

318 D < 16 mm), and the other was not considered on a particle size scale. The former data, expressed by

319 A and B (Type 1), were collected at two sites and reanalyzed by size (Fig. 4); the latter data, expressed

320 as C–E (Type 2), were collected at 18 sites (Table 2). Free-fall experiments on collected volcanic ash

321 particles were carried out in the large-scale rainfall simulator of the National Research Institute for

322 Earth Science and Disaster Prevention (NIED) in Tsukuba, Japan. The collected particles were dropped

323 manually by a manager around 17 m from the ground and re-collected by a third-generation 2DVD

324 (Maki et al., 2016). Half a cup of each sample was dropped for 30 s to stimulate dispersion, and the

325 measurement period was 1 min. To avoid wind effects including turbulence, the 2DVD was surrounded

326 by a 27 m^3 windbreaking wall (Fig. 5).

327 The free-fall experiments were conducted at intervals of 1 min over 6 h 30 min, as shown in Fig.

328 6. The number of particles detected by 2DVD was less than 10,000 for 1 min, and the particle size

329 range of The former data set (A, B) was proportional to its phi-scale, since small particles may be

330 observed in collisions or break-up from aggregates. Bonadonna et al. (2011) showed that the dominant

331 distribution areas of volcanic ash particles of $\Phi = 1\sim2$, $1\sim3$, and $3\sim9$ corresponded to around 10, 20,

332 and 30 km from the vent of Eyjafjallajökull, Iceland, respectively. Dellino et al. (2012) reported that

333 the dominant volcanic ash particle size is concentered at $\Phi = 0\sim3$ and $1\sim2$ at 3 and 9 km from the vent

334 of the same volcano, respectively. Based on these studies, the results of the present study represent the

335 range between 2 and 20 km from the vent under natural conditions.

336   Figure 7 shows the distribution of raw data (the number of data: 274,215) for V_T and γ with D.

337 There were various γ values, from 0 to 2, when the volume-equivalent particle $D < 2$ mm, and most of

338 the data were concentrated near 0. The γ values converged around 1 and their distributional range

339 decreased with D. It should be noted that this feature is different from that of raindrops, where smaller

340 raindrops converge around 1 and gradually decrease with D (Thurai and Bringi, 2005). Beard and

341 Chuang (1987) and Andsager et al. (1999) suggested that these raindrop features denote polynomial

342 relationships (Fig. 7a). The median value with a 0.25 mm D interval corresponded well to the center of

343 the data contour. The median line converged around $\gamma = 0.93$ based on the correlation coefficient

344 value (CC). When this was higher than 0.95 for each D interval, the data converged. According to this

345 condition, the range of $2 < D < 5$ mm was satisfied and the mean value was calculated using these data.

346   The V_T had a wider range when $D < 2$ mm but the median line corresponded well to the center of

347 the data (Fig. 7b). The line representing the largest amount of data is higher than the V_T of raindrops

348 suggested by Atlas et al. (1973), and lower than the volcanic ash discussed by Bonadonna et al. (2011).

349   To select a reliable range for particle D, a theoretical terminal velocity equation ($V_{T,Ref}$)

350 corresponding to Eqs. 2–7 was used as the reference. The particle density associated with the eruption

351 of Sakurajima volcano is between 2.43 and 2.59 g cm^{-3} (Oguchi et al., 2009), but the actual particles

352 contain air vacuoles (Van Eaton et al., 2012). This means that the bulk density, including vacuoles, is

353 smaller than the particle density. Therefore, the minimum particle density was considered to be 2.43 g

354 cm^{-3}, and this was used as an input parameter. The atmospheric conditions of T and P were considered

355 using ground observation data from automatic weather stations (AWS), supported by the JMA. The

356 falling height of a particle when D = 4 was lower than that under laboratory conditions when it reached

357 90% of V_T (13.9 m) (17 m); therefore, the available data range is considered to be D ≤ 4 mm, and this

358 would satisfy a steady-state oscillation. The detailed equations used in the present study are shown in

359 Appendix A.

360

361

362 **f. Quality control procedures**

363 The 2DVD was originally developed to detect raindrop hydrometeors. For this reason, additional

364 quality control (QC) checks were deemed necessary to ensure applicability to non-hydrometeors, such

365 as volcanic ash particles. Specifically, we performed the following two QC procedures for accurate

366 analysis of the data:

367 i) Particle D > 0.25 mm was selected in consideration of the minimum spatial resolution of 2DVD.

368 ii) If the major axis observed by 2DVD was 10% longer than that of the value calculated directly

369 based on data coordinates, the data were considered erroneous and thus removed. A 10% bias range

370 was considered based on mathematical error, the irregular particle shape, and the limitation of the

371 spatiotemporal resolution of 2DVD.

372 iii) Based on the definition of β (Fig. 2), the perfect condition with respect to ellipsoids is satisfied

373 when |β| = 0º (90º) for OH and PV (OV and PH); these values are defined as the center values. However,

374 2DVD calculated that the β for each particle shape type was concentrated around |β| = 0º (90º) with

375 respect to horizontally (vertically) oriented particles, which correspond to OH and PH (OV and PV).

376 Furthermore, analysis of particles with an orthogonal center angle from 0º is difficult, since they have

377 two center angles (±90º). To address observation errors and enhance the convenience of analysis, all

378 center angles were set to $|\beta| = 0º$ and modified to give the representative canting angle, β_R, using the

379 following equation:

380

381 $$\beta_R = \beta - \beta_0$$

382

383 where β_0 is the orienting angle, defined by the central angle of oscillation. In the case of vertically

384 oriented particles (OV and PV), β_0 could be defined as ±90º. The sign of β_0 follows that of β. After

385 selecting the particle shape types and applying these QC procedures, 19.31% of the data (62,953)

386 remained (Table 1).

387

388

3. Results

390

a. Size and shape distribution

The particle size distribution over the entire volcanic ash sample was skewed leftward, and the particle shape distribution differed with particle size (Fig. 8). The particles were predominantly horizontally oriented (75.51%) or vertically oriented (21.60%). Oblate and prolate spheroids made up 76.26% and 23.85% of the particles, respectively. Hence, the particles were mainly OH (57.38%) or PH (15.88%) (Table 2). The particles were predominantly $0.25 < D < 0.5$ mm (63.00%) or $0.5 < D < 1$ mm (32.80%). Relatively few particles had $D > 1$ mm (4.20%).

There was large variation in shape among particles $0.25 < D < 0.5$ mm, but the variation decreased with increasing D. All of the particle shape types had the largest number of particle at $D > 1.0$ mm and the next were shown at $0.5 < D < 1.0$ mm, except for OH. In total, 95.80% of OH particles had $D < 1$ mm; at $D < 0.5$ mm, the value was 75.68%, and at $D = 0.5$–1 mm, it was 22.36%. In the cases of PH and OV, 93.63% and 93.87% of these particles, respectively, had $D < 1$ mm. Beyond $D > 1$ mm, the differences in the number of particles for each particle shape type were considerably decreased. The PSD of volcanic ash particles depended on the distance from the vent (Beckett et al., 2015; Stevenson et al., 2015). Based on the results, this particle size and shape distribution would represent the area located over 2–20 km from the vent.

407

408

b. Terminal velocity

It is difficult to apply qualitative analysis approaches to V_T since it depends on the scale, magnitude, and duration of an eruption. Furthermore, it is impossible to develop a model of V_T without knowledge

412 of the aerodynamic properties of the volcanic ash particles, since V_T is a function of the density, shapes,

413 and oscillations of particles. In this study, we analyzed the basic features of volcanic ash particles in a

414 laboratory experiment to obtain reliable results.

415   The observed values of V_T were well classified by particle shape and were generally higher than

416 those of raindrops, as previously suggested by Atlas et al. (1973) (Fig. 9). The values were estimated

417 using a multiple regression analysis, with V_T defined for each particle type, and with additional QC

418 measures applied. If we consider a single V_T QC measure for the entire particle types, a number of

419 available data might be removed, since V_T critically depends on particle shape. Therefore, we applied

420 a ±60% V_T QC threshold (Jaffrain et al., 2011).

421   The highest values of V_T were recorded in the order of prolate, sphere, and oblate. Vertically

422 oriented particles had higher V_T values than horizontal ones. For raindrops with a single particle shape

423 type, V_T changes with atmospheric conditions, especially vertical air motion (Kim and Lee, 2016).

424 However, the V_T values for volcanic ash particles change independent of external conditions, since

425 they have various particle shapes. The V_T for every particle type was considered to be in a power-law

426 form, except for OH. OH particles followed the regression line relatively closely, and showed the

427 highest CC and root mean square error (RMSE) values, of 0.94 and 0.46 m s^{-1}, respectively.

428 Horizontally orientated particles had relatively higher correlations (OH: 0.94, PH: 0.87) compared to

429 those with a vertical orientation (OV: 0.75, PV: 0.71). All of these data are summarized in Table 3.

430   To verify the reliability of the particle data obtained by 2DVD, which was originally developed to

431 detect liquid raindrops, particle density, C_D, and Re, as well as theoretical V_T values according to these

432 parameters, were analyzed. To calculate the parameters of interest, including the surface area and

433 cross-sectional area of irregular particles, we applied the irregular particle volume estimation equations

434 of Huang et al. (2010).

435

c. Aerodynamic properties

Particle densities were estimated using the $V_{T,Ref}$, converged to 2.37 g cm^{-3} when D < 1.5 mm (Fig. 10a). This value corresponds well to that of the minimum particle density (2.44 g cm^{-3}) reported by Oguchi et al. (2009). The slight difference is likely due to observation errors and the presence of vesicles (e.g., Seligman et al., 2016). The median value of particle density is changed to 0.5 < D < 1.5 mm, and this range corresponds to that of V_T. Horizontally oriented particles (OH and PH) have relatively smaller particle density and vertically oriented particles (OV and PV) have higher density (Fig. 10b); spheres have particle densities that accord best with D. The median particle density values for all particle shapes converged when D < 2 mm, and the converged particle density values ranged from 2.35 to 2.50 g cm^{-3}.

The Re and C_D for the all particle shapes ranged from 10 to 4,000 and 0.6 to 20, respectively (Fig. 11a). Higher values of C_D were observed when Re < 70; above this threshold, C_D dramatically decreased. These results were derived according to the number of OH particles, which mainly had D < 0.5 mm, and had higher C_D and lower Re. Particle shape was divided into two types: OH and others (Fig. 11b). OH particles had higher C_D compared to the other particle shapes, which in turn showed few differences among themselves. The OH particles experience strong drag forces under the same flow conditions, leading to lower V_T. The differences between OH and other particles diminished with Re < 1,000. The other particle shapes had relatively higher C_D in the range 10 < Re < 3,000. Rong et al. (2015) analyzed the relationship between Re and C_D for oblate and prolate particles, and showed that OH particles had higher C_D compared to the reference line (Clift and Gauven, 1971) in the range 0 < Re < 400. Each relationship is summarized in Fig. 11.

d. Axis ratio

The γ of a particle affects the backscattering power of electromagnetic waves, and it is necessary to calculate the horizontal reflectivity (Z in dBZ), differential reflectivity (Z_{DR} in dB), and specific differential polarization phase shift (K_{DP} in ° km^{-1}). Note that previous studies have analyzed the γ distribution for raindrops and snow, including hail; however few studies have been reported on volcanic ash.

Smaller raindrop particles exhibit higher values of σ. However, most of the particles are concentrated around $\gamma = 1$ when D is close to 0 mm, and the γ for raindrops was shown to be inversely proportional to D (e.g., Pruppacher and Beard, 1970; Beard and Chuang, 1987; Goddard et al. 1994b; Andsager et al. 1999; Thurai and Bringi, 2005). Snowflakes showed linear relationships of γ and D that were different from those of raindrops. Brandes et al. (2007) suggested that an equation for γ where (D) = 0.01714D + 0.8467. Hail had a similar γ to snowflakes, of 0.77 (Matson and Huggins, 1980) versus $0.75 < \gamma < 0.79$ (Jewell and Brimelow, 2009), respectively.

Figure 12 shows the quartiles and median values of γ for the entire particle shapes, and for each individual particle shape type. The γ had a higher standard deviation (σ_γ) of > 0.25 when $D < 0.75$ mm, which decreased and converged to $\sigma_\gamma = 0.15$ when $D > 1$ mm (Fig. 12a). The γ in the lower σ_γ range converged to $\gamma = 0.94$ and could be expressed as follows:

$$\gamma(D) = 0.94 - 0.25\exp(-1.90\ D)$$

Eq. (8)

The particles are more easily classified by shape than by V_T (Fig. 12b). Every particle shape type was independent of D, except for OH. The relationships of the particle shape types are expressed as follows (Eqs. 9–12):

$$\gamma(D)_{OH} = 0.37\tanh(1.84D - 1.88) + 0.38$$

484

485   Eq. (9)

$$\gamma_{OV} = 1.15$$

486

487   Eq. (10)

$$\gamma_{PH} = 0.88$$

488

489   Eq. (11)

$$\gamma_{PV} = 1.24$$

490

491   Eq. (12)

492

493   The parameter $\gamma(D)_{OH}$ was calculated using the hyperbolic tangent (tanh) for the following reasons:

494   i) its range of values was wider than those of other particle types; ii) the data distribution changed

495   continuously with D; and iii) it was present in a higher proportion (30.44%) compared to the other

496   parameters. We found that variations in γ decreased with D and the proportion of Sp shapes increased

497   when D > 2 mm. The particle types OV and PH showed a wide distribution over $1 < \gamma < 1.5$ and $0.4 <$

498     $\gamma < 1.0$, respectively, when D < 2 mm, but the variability in median values was relatively low. The

499   relationships of γ for each particle shape type could be expressed by constant values at $\gamma = 0.75$ (OH),

500   0.88 (PH), 1.15 (OV), and 1.24 (PV), respectively, and these differences are around $\gamma = 0.12$. Maki et

501   al. (2014) analyzed dual-pol radar variables and found that Z_{DR} increased with time; the dominant

502   values at 10 and 18 min after the eruption were close to 1 and 2 dB, respectively. With respect to

503   hydrometeors, the dominant γ of volcanic ash can be inferred from the relationship between γ and Z_{DR},

504   as suggested by Herzegh and Jameson (1992). The values correspond to the γ of volcanic ash when the

505   median γ of rain and ice is 0.85 and 0.73, respectively; this assumption is based on the $|K|^2$ for

506   volcanic ash being between that of ice and liquid water. These representative values correspond to D

507 of 1 and 0.15 mm, respectively, based on Eq. 9. It is implied that the amount of particles was largest

508 when D < 1 mm (95.8%) and the γ corresponded well to the observed Z_{DR}.

509

510

511 **e. Canting angle**

512 Statistical analysis of β is required to understand the aerodynamic properties of volcanic ash

513 particles, and the input parameters of T-matrix scattering simulations, to verify the observed radar

514 variables. A histogram was used to analyze the distribution and dominant characteristics of β_R. The

515 interval of the histogram was set to 4º.

516 More than 95% of β values for each particle shape type were concentrated in the range $|\beta_R| \leq 30^\circ$,

517 with 0º as the center (Fig. 13). The particles were symmetrically distributed around 0º and more than

518 50% were concentrated in the range $|\beta_R| < 4^\circ$. The horizontally oriented β distribution was relatively

519 narrow ($|\beta_R| < 20^\circ$) and exhibited a unimodal distribution. It is noteworthy that 90% of OH particles

520 were concentrated in the range $|\beta_R| < 4^\circ$. The vertically oriented β distribution was relatively broader

521 ($|\beta_R| < 30^\circ$) and followed a bimodal distribution. PV exhibited a bimodal form, but this was not

522 symmetrical about 0º. For spheres, the β distribution was narrower, similar to horizontally oriented

523 particles, and its had a bimodal distribution, similar to vertically oriented particles, indicating that the

524 independent features of both orientations were combined.

525 The values of $|\overline{\beta_R}|$ and $|\sigma_\beta|$ for OH and PV (OV, PH) were 0º and 3.5º (0.4º, 13.1º), and 1.3º and

526 12.7º (0.2º, 10.9º), respectively. OV (OH) had the highest (lowest) value of $|\sigma_\beta|$. Thus, $|\overline{\beta_R}|$ and $|\sigma_\beta|$ for

527 the all volcanic ash particles were quite similar (0.3º and 10.1º, respectively) to those of raindrops and

528 the value of $|\sigma_\beta|$ for Sp (11.5°) was higher than that of the entire data set (10.1°).

529 In the case OH, the $|\sigma_\beta|$ value was about half that for raindrops while the values for OV, PH, and

530 PV particles were all similar to that of raindrops. This validates the assumption of Marzano et al. (2012)

531   under stable conditions ($|\sigma_\beta| = 10°$). Therefore, we assumed that the tumbling phenomenon ($|\sigma_\beta| > 30°$)

532   of the particles under calm atmospheric conditions was likely to be minor.

533   To analyze the correlation between particle D and β, quartiles for each particle D interval were

534   calculated (Fig. 14). The particles were concentrated at $|\beta_R| < 30°$ regardless of D, and median values

535   were stable when D < 1 mm for the entire particle shape types; however, fluctuation increased with D

536   (Fig. 14a). The $|\sigma_\beta|$ values gradually increased from 10° to 13° when $0.3 < D < 1.3$ mm and variability

537   was greatest around the center (13°). This increase in $|\sigma_\beta|$ would not be expected in the case of a

538   relatively small number of particles (Fig. 8a), since their standard deviation is largely maintained at

539   about 13° regardless of dataset size.

540   Variability in the median values for individual particles was more apparent. The values converged

541   around 0° but fluctuation increased with greater D from the zero line. The median $|\beta_R|$ values

542   exceeded   3°, 5°, 10°, and 15° when D > 1 mm, $1 < D < 2$ mm, $2 < D < 3$ mm, and D > 3 mm,

543   respectively (Fig. 14b).

544

545

546   **e. Verification**

547   To verify the basic parameters of volcanic ash estimated in the present study, the $V_{T, Ref}$ (Eq. 2) was

548   compared to the observed values (V_T) obtained in the free-fall experiments (Fig. 15). The particle

549   density (Fig. 10) and γ (Fig. 12) estimated in the present study were applied to the C_D (Eq. 3) and the

550   sphericity (Eqs. 5–7) relationships; these parameters were used as input values for $V_{T, Ref}$. The

551   atmospheric conditions were the same as in Fig. 5.

552   There was wide range of V_T over $0.25 < D < 1.2$ mm for the entire particle shape types, and V_T

553   decreased when D > 1.2 mm. The V_T in the present study corresponds to that obtained by Miwa et al

554   (2015), who analyzed Parsivel data using the same laboratory experiments (Fig. 5); correspondence

555 was also good with other previous results (Beckett et al., 2015). A polynomial regression analysis was

556 used to explore the nonlinear relationship between V_T and D (Table 3). The inflection point of V_T at

557 $0.7 < D < 1.3$ mm results from an increase in the number of OH when $D < 1$ mm (Fig. 8).

558   The $V_{T,Ref}$ was lower (higher) than the observed value when $D < 1.2$ mm ($D > 2.4$ mm). One of the

559 reasons why a difference between the theoretical and observed values appeared when $D > 2.4$ mm was

560 that the upper limit of D when 90% of the terminal velocity was reached was set at 4 mm for a height

561 of 17 m (Fig. A1). This is nonetheless meaningful because the values of $V_{T,\,Ref}$ calculated based on the

562 basic parameters in this study were within ±5% of the observed value.

563

4. Summary and Conclusions

To inform the development of QAE methods, basic parameters (V_T, γ and β) of volcanic ash particles were analyzed using 2DVD. Data were collected according to 18 automatic volcanic ash weight measurements performed on Sakurajima volcano, Japan (31.58º N, 130.65º E). To identify the aerodynamic properties of the volcanic ash particles in the samples, a free-fall experiment using 2DVD was conducted with the large-scale rainfall simulator of the NIED, and 274,215 raw data points were obtained.

Radar variables are highly dependent on the $|K|^2$, size, and shape of particles. Particle types with rotating symmetric axes were selected, because volcanic ash particles have a wide variety of irregular shapes. Their orientation was also considered, and horizontally (OH) and vertically (OV) oriented oblate spheroids were therefore studied, as well as horizontally (PH) and vertically (PV) oriented prolate spheroids, and spheres (Sp).

The particle shape types were defined according to their γ_T, with a 10% bias range; the β among two values was selected to be representative when the value of γ_T was smaller (larger) than that of the other observation direction in the case of the oblate (prolate) particle.

The dominant particle shape comprised horizontally and vertical oriented particles, present in proportions of 75.51% and 21.60%, respectively. Regarding particle shape, oblate (prolate) spheroids comprised 76.26% (23.85%) of all particles in the samples. The most common particle shape type was OH, accounting for 59% of all particles when $D < 1$ mm, and 69% when $D < 0.5$ mm. Overall, 95.80%, 93.87%, and 93.63% of the OH, OV, and PH particles had $D < 1$ mm, respectively.

The V_T of the particles were in the order of prolate, sphere, and oblate, and vertical oriented particles had higher V_T than horizontal orientated particles. These results are consistent with the $V_{T, Ref}$, which suggests that 2DVD is a reliable for observing volcanic ash particles and the tumbling phenomenon under stable weather conditions. A noticeable increase in V_T for OH in the range $0.5 < D$

588   < 1 mm occurred through an increase in γ and a decrease in the number of OH when D ~0.7 mm; this

589   was not observed for other particle types.

590   The estimated ρ_s converged to 2.37g cm^{-3} when D > 1.5 mm, and the median value changed over

591   the range 0.5 < D < 1.5 mm. This is consistent with the particle density value for the Sakurajima

592   volcano reported by Oguchi et al. (2009). The distributions of C_D and Re were divided into two particle

593   type categories, OH and other, and C_D increased dramatically when Re < 70. These results were derived

594   from the particle concentration of OH, which was highest when D < 0.5 mm; at this threshold, C_D was

595   higher and Re was lower. The range of V_T over 0.7 < D < 1.3 mm was informed by both γ and particle

596   density.

597   The σ_γ decreased when D > 0.75 mm, to 0.15, and converged to $\gamma = 0.94$. This is in contrast to the

598   results obtained for raindrops, but is highly consistent with results for actual eruptions. Most measured

599   values of Z_{DR} for Sakurajima volcanic ash clouds on August 18, 2013 were in the range 1–2 dB,

600   corresponding to a horizontally oriented oblate spheroid.

601   The $|\sigma_\beta|$ of OV particles with $|\beta_0| = 90°$ was largest (13.1°) among all particle types. OH particles

602   had the lowest $|\sigma_\beta|$ at 3.5°, and this value was also smaller than that of raindrops (7°–10°). Based on the

603    $|\sigma_\beta|$ results, the tumbling phenomenon would not be dominant under calm atmospheric conditions. The

604   quartiles were stable when D < 1 mm for the entire particle shape types, but increased with D. The

605   value of σ_β was higher when D < 1.3 mm and started to converge around 13° due to a decrease in the

606   number of OH particles.

607   The estimated γ and ρ_s were applied to the $V_{T,Ref}$ for validation. The observed V_T was within ±5%

608   of the theoretical value when D ≤ 4 mm, implying that the estimates of the basic parameters were

609   reasonable for the particle range considered.

610   These results could inform the development of new approaches for detecting non-hydrometeors

611   using weather radar, thus facilitating observations of ash clouds and preventing the damage to human

612   life and property caused by large amounts of ash fall. In future work, we will analyze the eruption of

613   Sakurajima volcano that occurred on August 18, 2013 with a dual-pol radar and 2DVD, using basic

614   parameters of volcanic ash particles obtained from laboratory experiments. Differences in

615   characteristics between the experimental, and actual basic parameters, and PSD, will be investigated.

616

Acknowledgments

617

618   This work was supported by a Grant-in Aid for JSPS KAKENHI (grant number JP16H03145) and

619   partially supported by a DPRI collaborative research grant (Kyoto Univ. 25G-11). The authors

620   acknowledge the provision of ashfall data and funding for this work from Kyoto and Kagoshima

621   Universities. The 2DVD data were provided by MEXT, Japan. We also thank the NIED for use of

622   their large-rainfall simulator.

623

624   **Appendix A**

625

626   The theoretical fall velocity and falling distance with time are calculated as follows;

627

628
$$F = ma = F_g - F_D$$

629   Eq. (A1)

630
$$F_g = mg$$

631   Eq. (A2)

632
$$F_D = \frac{1}{2}\rho_g V^2 C_D A$$

633   Eq. (A3)

634

635   where F_g is universal gravitation, F_D is drag force, m is mass, and a is the free-fall acceleration.

636   In Eq. A2, g is the acceleration due to gravity, considered to be 9.81 m s^{-2}, and V and C_D in Eq. A3

637   correspond to the values in Eq. 2–7. The symbols μ and ρ_g are the dynamic viscosity and density of

638   the atmosphere and were assumed as 1.837×10^{-5} kg m^{-1} s^{-1} and 1.194×10^{-5} g cm^{-3}, respectively.

639   The results were based on conditions at an atmospheric T as 25 °C.

640   To ensure accuracy, we considered the surface roughness effect of a volcanic ash particle (1.07^{-1})

641   on the fall velocity, as suggested by Bagheri and Bonadonna (2016), and the results for D = 4 mm

642   are shown in Fig. A1.

643 **References**

644

645 Adams, R. J., Perger, W. F., Rose, W. I., and Kostinski, A.: Measurements of the complex dielectric
646   constant of volcanic ash from 4 to 19 GHz, Journal of Geophysical Research: Solid Earth,
647   101, 8175-8185, 1996.

648 Alfano, F., Bonadonna, C., Delmelle, P., and Costantini, L.: Insights on tephra settling velocity from
649   morphological observations, Journal of Volcanology and Geothermal Research, 208, 86-
650   98, 2011.

651 Andsager, K., Beard, K. V., and Laird, N. F.: Laboratory measurements of axis ratios for large
652   raindrops, Journal of the Atmospheric Sciences, 56, 2673-2683, 1999.

653 Atlas, D., Srivastava, R., and Sekhon, R. S.: Doppler radar characteristics of precipitation at vertical
654   incidence, Reviews of Geophysics, 11, 1-35, 1973.

655 Böhm, H. P.: A general equation for the terminal fall speed of solid hydrometeors, Journal of the
656   Atmospheric Sciences, 46, 2419-2427, 1989.

657 Bagheri, G. and Bonadonna, C.: On the drag of freely falling non-spherical particles, Powder
658   Technology, 301, 526-544, 2016.

659 Bagheri, G., Bonadonna, C., Manzella, I., Pontelandolfo, P., and Haas, P.: Dedicated vertical wind
660   tunnel for the study of sedimentation of non-spherical particles, Review of Scientific
661   Instruments, 84, 054501, 2013.

662 Beard, K. V. and Chuang, C.: A new model for the equilibrium shape of raindrops, Journal of the
663   Atmospheric sciences, 44, 1509-1524, 1987.

664 Beckett, F., Witham, C., Hort, M., Stevenson, J., Bonadonna, C., and Millington, S.: Sensitivity of

665   dispersion model forecasts of volcanic ash clouds to the physical characteristics of the

666   particles, Journal of Geophysical Research: Atmospheres, 120, 2015.

667 Bonadonna, C., Cioni, R., Pistolesi, M., Elissondo, M., and Baumann, V.: Sedimentation of long-

668   lasting wind-affected volcanic plumes: the example of the 2011 rhyolitic Cordón Caulle

669   eruption, Chile, Bulletin of Volcanology, 77, 13, 2015.

670 Bonadonna, C., Ernst, G., and Sparks, R.: Thickness variations and volume estimates of tephra fall

671   deposits: the importance of particle Reynolds number, Journal of Volcanology and

672   Geothermal Research, 81, 173-187, 1998.

673 Bonadonna, C., Folch, A., Loughlin, S., and Puempel, H.: Future developments in modelling and

674   monitoring of volcanic ash clouds: outcomes from the first IAVCEI-WMO workshop on

675   Ash Dispersal Forecast and Civil Aviation, Bulletin of volcanology, 74, 1-10, 2012.

676 Bonadonna, C., Genco, R., Gouhier, M., Pistolesi, M., Cioni, R., Alfano, F., Hoskuldsson, A., and

677   Ripepe, M.: Tephra sedimentation during the 2010 Eyjafjallajökull eruption (Iceland)

678   from deposit, radar, and satellite observations, Journal of Geophysical Research: Solid

679   Earth (1978–2012), 116, 2011.

680 Brandes, E. A., Ikeda, K., Zhang, G., Schönhuber, M., and Rasmussen, R. M.: A statistical and physical

681   description of hydrometeor distributions in Colorado snowstorms using a video

682   disdrometer, Journal of applied meteorology and climatology, 46, 634-650, 2007.

683 Clift, R. and Gauvin, W.: Motion of particles in turbulent gas streams, British Chemical Engineering,

684   16, 229-&, 1971.

685   Coltelli, M., Miraglia, L., and Scollo, S.: Characterization of shape and terminal velocity of tephra

686   particles erupted during the 2002 eruption of Etna volcano, Italy, Bulletin of volcanology,

687   70, 1103-1112, 2008.

688   Del Bello, E., Taddeucci, J., Vitturi, M. d. M., Scarlato, P., Andronico, D., Scollo, S., Kueppers, U.,

689   and Ricci, T.: Effect of particle volume fraction on the settling velocity of volcanic ash

690   particles: insights from joint experimental and numerical simulations, Scientific reports,

691   7, 39620, 2017.

692   Dellino, P., Gudmundsson, M., Larsen, G., Mele, D., Stevenson, J., Thordarson, T., and Zimanowski,

693   B.: Ash from the Eyjafjallajökull eruption (Iceland): Fragmentation processes and

694   aerodynamic behavior, Journal of Geophysical Research: Solid Earth, 117, 2012.

695   Dellino, P., Mele, D., Bonasia, R., Braia, G., La Volpe, L., and Sulpizio, R.: The analysis of the

696   influence of pumice shape on its terminal velocity, Geophysical Research Letters, 32,

697   2005.

698   Dioguardi, F., Mele, D., and Dellino, P.: A New One-Equation Model of Fluid Drag for Irregularly

699   Shaped Particles Valid Over a Wide Range of Reynolds Number, Journal of Geophysical

700   Research: Solid Earth, 123, 144-156, 2018.

701   Dioguardi, F., Mele, D., Dellino, P., and Dürig, T.: The terminal velocity of volcanic particles with

702   shape obtained from 3D X-ray microtomography, Journal of Volcanology and Geothermal

703   Research, 329, 41-53, 2017.

704   Donnadieu, F.: Volcanological applications of Doppler radars: A review and examples from a

705   transportable pulse radar in L-band, INTECH Open Access Publisher, 2012.

706 Folch, A.: A review of tephra transport and dispersal models: evolution, current status, and future

707   perspectives, Journal of Volcanology and Geothermal Research, 235, 96-115, 2012.

708 Folch, A., Costa, A., and Macedonio, G.: FALL3D: A computational model for transport and

709   deposition of volcanic ash, Computers & Geosciences, 35, 1334-1342, 2009.

710 Ganser, G. H.: A rational approach to drag prediction of spherical and nonspherical particles, Powder

711   Technology, 77, 143-152, 1993.

712 Garboczi, E. and Bullard, J.: 3D analytical mathematical models of random star-shape particles via a

713   combination of X-ray computed microtomography and spherical harmonic analysis,

714   Advanced Powder Technology, 28, 325-339, 2017.

715 Garrett, T. J., Yuter, S. E., Fallgatter, C., Shkurko, K., Rhodes, S. R., and Endries, J. L.: Orientations

716   and aspect ratios of falling snow, Geophysical Research Letters, 42, 4617-4622, 2015.

717 Goddard, C. and Wierzbicka, A.: Semantic and lexical universals: Theory and empirical findings, John

718   Benjamins Publishing, 1994.

719 Hölzer, A. and Sommerfeld, M.: New simple correlation formula for the drag coefficient of non-

720   spherical particles, Powder Technology, 184, 361-365, 2008.

721 Haider, A. and Levenspiel, O.: Drag coefficient and terminal velocity of spherical and nonspherical

722   particles, Powder technology, 58, 63-70, 1989.

723 Happel, J. and Brenner, H.: Low Reynolds number hydrodynamics: with special applications to

724   particulate media, Springer Science & Business Media, 2012.

725 Harris, D. M. and Rose, W. I.: Estimating particle sizes, concentrations, and total mass of ash in

726   volcanic clouds using weather radar, Journal of Geophysical Research: Oceans (1978–

727   2012), 88, 10969-10983, 1983.

728 Hendry, A., Antar, Y., and McCormick, G.: On the relationship between the degree of preferred

729 orientation in precipitation and dual-polarization radar echo characteristics, Radio science,

730 22, 37-50, 1987.

731 Herzegh, P. H. and Jameson, A. R.: Observing precipitation through dual-polarization radar

732 measurements, Bulletin of the American Meteorological Society, 73, 1365-1376, 1992.

733 Hillman, S. E., Horwell, C. J., Densmore, A. L., Damby, D. E., Fubini, B., Ishimine, Y., and Tomatis,

734 M.: Sakurajima volcano: a physico-chemical study of the health consequences of long-

735 term exposure to volcanic ash, Bulletin of volcanology, 74, 913-930, 2012.

736 Huang, G.-J., Bringi, V., Cifelli, R., Hudak, D., and Petersen, W.: A methodology to derive radar

737 reflectivity-liquid equivalent snow rate relations using C-band radar and a 2D video

738 disdrometer, Journal of Atmospheric and Oceanic Technology, 27, 637-651, 2010.

739 Huang, G.-J., Bringi, V., Moisseev, D., Petersen, W. A., Bliven, L., and Hudak, D.: Use of 2D-video

740 disdrometer to derive mean density–size and Z e–SR relations: Four snow cases from the

741 light precipitation validation experiment, Atmospheric Research, 153, 34-48, 2015.

742 Huang, G.-J., Bringi, V., and Thurai, M.: Orientation angle distributions of drops after an 80-m fall

743 using a 2D video disdrometer, Journal of Atmospheric and Oceanic Technology, 25, 1717-

744 1723, 2008.

745 Jaffrain, J., Studzinski, A., and Berne, A.: A network of disdrometers to quantify the small-scale

746 variability of the raindrop size distribution, Water Resources Research, 47, 2011.

747 Jewell, R. and Brimelow, J.: Evaluation of Alberta hail growth model using severe hail proximity

748 soundings from the United States, Weather and Forecasting, 24, 1592-1609, 2009.

749   Jung, Y., Zhang, G., and Xue, M.: Assimilation of simulated polarimetric radar data for a convective

750   storm using the ensemble Kalman filter. Part I: Observation operators for reflectivity and

751   polarimetric variables, Monthly Weather Review, 136, 2228-2245, 2008.

752   Kanofsky, L. M.: A comparative study of drop size distribution retrieval using two video disdrometers

753   and a UHF wind profiling radar, 2005.

754   Kim, D. K. and Lee, D. I.: Raindrop size distribution properties associated with vertical air motion in

755   the stratiform region of a springtime rain event from 1290 MHz wind profiler, micro rain

756   radar and Parsivel disdrometer measurements, Meteorological Applications, 23, 40-49,

757   2016.

758   Kruger, A. and Krajewski, W. F.: Two-dimensional video disdrometer: A description, Journal of

759   Atmospheric and Oceanic Technology, 19, 602-617, 2002.

760   Kunii, D.: 0. Levenspiel, Fluidization Engineering, John Wiley, 8, 44-45, 1969.

761   Langmann, B., Folch, A., Hensch, M., and Matthias, V.: Volcanic ash over Europe during the eruption

762   of Eyjafjallajökull on Iceland, April–May 2010, Atmospheric Environment, 48, 1-8, 2012.

763   Maki, M. and Doviak, R.: Volcanic ash size distribution determined by weather radar, 2001, 1810-

764   1811.

765   Maki, M., Iguchi, M., Maesaka, T., Miwa, T., Tanada, T., Kozono, T., Momotani, T., Yamaji, A., and

766   Kakimoto, I.: Preliminary results of weather radar observations of sakurajima volcanic

767   smoke, Journal of Disaster Research, 11, 15-30, 2016.

768   Maki, M., Maesaka, T., Kozono, T., Nagai, M., Furukawa, R., Nakada, S., Koshida, T., and Takenaka,

769   H.: Quantitative volcanic ash estimation by operational polarimetric weather radar, 2012.

770   Maki, M., Maesaka, T., Muraji, Y., and Suzuki, I.: Statistical analysis of volcanic ash measured by X-

771   band polarimetric radar, 2014.

772   Mandø, M. and Rosendahl, L.: On the motion of non-spherical particles at high Reynolds number,

773   Powder Technology, 202, 1-13, 2010.

774   Marzano, F. S., Barbieri, S., Vulpiani, G., and Rose, W. I.: Volcanic ash cloud retrieval by ground-

775   based microwave weather radar, IEEE transactions on geoscience and remote sensing, 44,

776   3235-3246, 2006.

777   Marzano, F. S., Picciotti, E., Montopoli, M., and Vulpiani, G.: Inside volcanic clouds: Remote sensing

778   of ash plumes using microwave weather radars, Bulletin of the American Meteorological

779   Society, 94, 1567-1586, 2013.

780   Marzano, F. S., Picciotti, E., Vulpiani, G., and Montopoli, M.: Synthetic signatures of volcanic ash

781   cloud particles from X-band dual-polarization radar, IEEE Transactions on Geoscience

782   and Remote Sensing, 50, 193-211, 2012.

783   Matson, R. J. and Huggins, A. W.: The direct measurement of the sizes, shapes and kinematics of

784   falling hailstones, Journal of the Atmospheric Sciences, 37, 1107-1125, 1980.

785   Nešpor, V., Krajewski, W. F., and Kruger, A.: Wind-induced error of raindrop size distribution

786   measurement using a two-dimensional video disdrometer, Journal of Atmospheric and

787   Oceanic Technology, 17, 1483-1492, 2000.

788   Miwa T., Maki M., Kozono T., Fujita E., Tanada T., and Iguchi M.: Experimental measurement on

789   falling velocity of volcanic ash from Sakurajima volcano by using PARSIVEL

790   disdrometer. Annual of Disas. Prev. Res. Inst., Kyoto Univ. 58(B), 91-94, 2015.

791   Oguchi, T., Udagawa, M., Nanba, N., Maki, M., and Ishimine, Y.: Measurements of dielectric constant

792   of volcanic ash erupted from five volcanoes in Japan, IEEE Transactions on Geoscience

793   and Remote Sensing, 47, 1089-1096, 2009.

794   Poulidis, A. P., Takemi, T., Iguchi, M., and Renfrew, I. A.: Orographic effects on the transport and

795   deposition of volcanic ash: A case study of Mount Sakurajima, Japan, Journal of

796   Geophysical Research: Atmospheres, 122, 9332-9350, 2017.

797   Pruppacher, H. R. and Beard, K.: A wind tunnel investigation of the internal circulation and shape of

798   water drops falling at terminal velocity in air, Quarterly Journal of the Royal

799   Meteorological Society, 96, 247-256, 1970.

800   Riley, C. M., Rose, W. I., and Bluth, G. J.: Quantitative shape measurements of distal volcanic ash,

801   Journal of Geophysical Research: Solid Earth, 108, 2003.

802   Rong, L., Zhou, Z., and Yu, A.: Lattice–Boltzmann simulation of fluid flow through packed beds of

803   uniform ellipsoids, Powder Technology, 285, 146-156, 2015.

804   Rosenfeld, D. and Ulbrich, C. W.: Cloud microphysical properties, processes, and rainfall estimation

805   opportunities. In: Radar and Atmospheric Science: A Collection of Essays in Honor of

806   David Atlas, Springer, 2003.

807   Ryzhkov, A., Pinsky, M., Pokrovsky, A., and Khain, A.: Polarimetric radar observation operator for a

808   cloud model with spectral microphysics, Journal of Applied Meteorology and

809   Climatology, 50, 873-894, 2011.

810   Sauvageot, H.: Radar meteorology, Artech House Publishers, 1992.

811   Seliga, T. A. and Bringi, V.: Potential use of radar differential reflectivity measurements at orthogonal

812   polarizations for measuring precipitation, Journal of Applied Meteorology, 15, 69-76,

813   1976.

814   Seligman, A. N., Bindeman, I. N., Watkins, J. M., and Ross, A. M.: Water in volcanic glass: From

815   volcanic degassing to secondary hydration, Geochimica et Cosmochimica Acta, 191, 216-

816   238, 2016.

817   Sigurdsson, H., Houghton, B., McNutt, S., Rymer, H., and Stix, J.: The encyclopedia of volcanoes,

818   Elsevier, 2015.

819   Sparks, R., Bursik, M., Carey, S., Gilbert, J., Glaze, L., Sigurdsson, H., and Woods, A.: Volcanic

820   Plumes, 574 pp. John Wiley, Chichester, UK, 1997.

821   Stevenson, J., Millington, S., Beckett, F., Swindles, G., and Thordarson, T.: Big grains go far:

822   understanding the discrepancy between tephrochronology and satellite infrared

823   measurements of volcanic ash, Atmospheric Measurement Techniques, 8, 2069-2091,

824   2015.

825   Stokes, G. G.: On the effect of the internal friction of fluids on the motion of pendulums, Pitt Press

826   Cambridge, 1851.

827   Suzuki, T.: A theoretical model for dispersion of tephra, Arc volcanism: physics and tectonics, 95, 113,

828   1983.

829   Tajima, Y., Ohara, D., Fukuda, K., and Shimomura, S.: Development of Automatic Tephrometer for

830   Monitoring of Volcano, 2015, 39-46.

831   Testud, J., Oury, S., Black, R. A., Amayenc, P., and Dou, X.: The concept of "normalized" distribution

832   to describe raindrop spectra: A tool for cloud physics and cloud remote sensing, Journal

833   of Applied Meteorology, 40, 1118-1140, 2001.

834   Thurai, M. and Bringi, V.: Drop axis ratios from a 2D video disdrometer, Journal of Atmospheric and

835   Oceanic Technology, 22, 966-978, 2005.

836   Thurai, M., Huang, G., Bringi, V., Randeu, W., and Schönhuber, M.: Drop shapes, model comparisons,

837   and calculations of polarimetric radar parameters in rain, Journal of Atmospheric and

838   Oceanic Technology, 24, 1019-1032, 2007.

839   Tokay, A., Wolff, D. B., and Petersen, W. A.: Evaluation of the new version of the laser-optical

840   disdrometer, OTT Parsivel2, Journal of Atmospheric and Oceanic Technology, 31, 1276-

841   1288, 2014.

842   Tran-Cong, S., Gay, M., and Michaelides, E. E.: Drag coefficients of irregularly shaped particles,

843   Powder Technology, 139, 21-32, 2004.

844   Ulbrich, C. W.: Natural variations in the analytical form of the raindrop size distribution, Journal of

845   Climate and Applied Meteorology, 22, 1764-1775, 1983.

846   Van Eaton, A. R., Muirhead, J. D., Wilson, C. J., and Cimarelli, C.: Growth of volcanic ash aggregates

847   in the presence of liquid water and ice: an experimental approach, Bulletin of volcanology,

848   74, 1963-1984, 2012.

849   Waterman, P.: Matrix formulation of electromagnetic scattering, Proceedings of the IEEE, 53, 805-

850   812, 1965.

851   Waterman, P. C.: Symmetry, unitarity, and geometry in electromagnetic scattering, Physical review D,

852   3, 825, 1971.

853   Wilson, L. and Huang, T.: The influence of shape on the atmospheric settling velocity of volcanic ash

854   particles, Earth and Planetary Science Letters, 44, 311-324, 1979.

855   Wilson, T. M., Jenkins, S., and Stewart, C.: Impacts from volcanic ash fall. In: Volcanic Hazards,

856   Risks and Disasters, Elsevier, 2015.

857   Wilson, T. M., Stewart, C., Sword-Daniels, V., Leonard, G. S., Johnston, D. M., Cole, J. W., Wardman,

858   J., Wilson, G., and Barnard, S. T.: Volcanic ash impacts on critical infrastructure, Physics

859   and Chemistry of the Earth, Parts A/B/C, 45, 5-23, 2012.

860
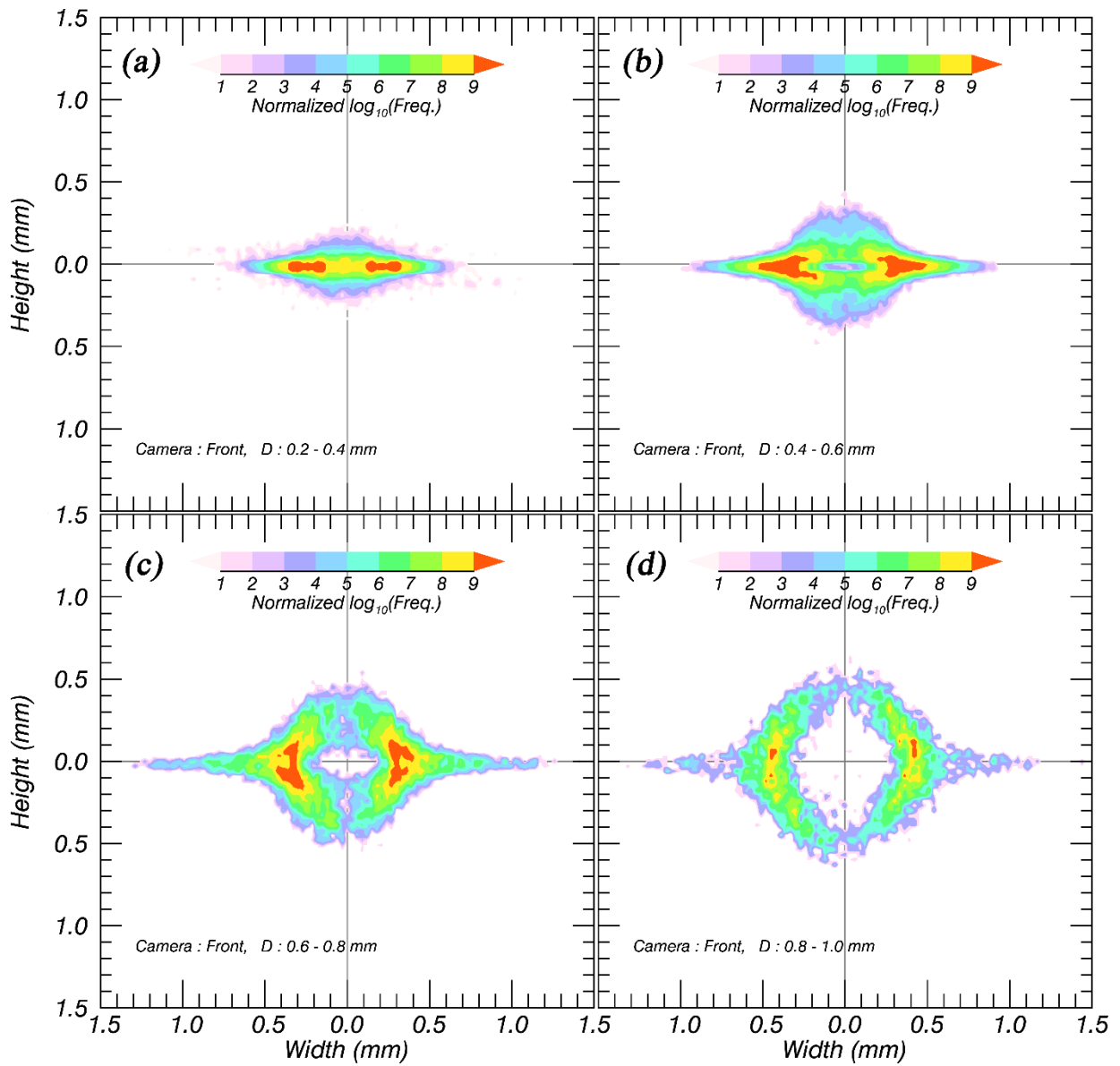
Figures

Figure 1. Accumulated contoured images of volcanic ash particles with D measured by a two-dimensional video disdrometer (2DVD).
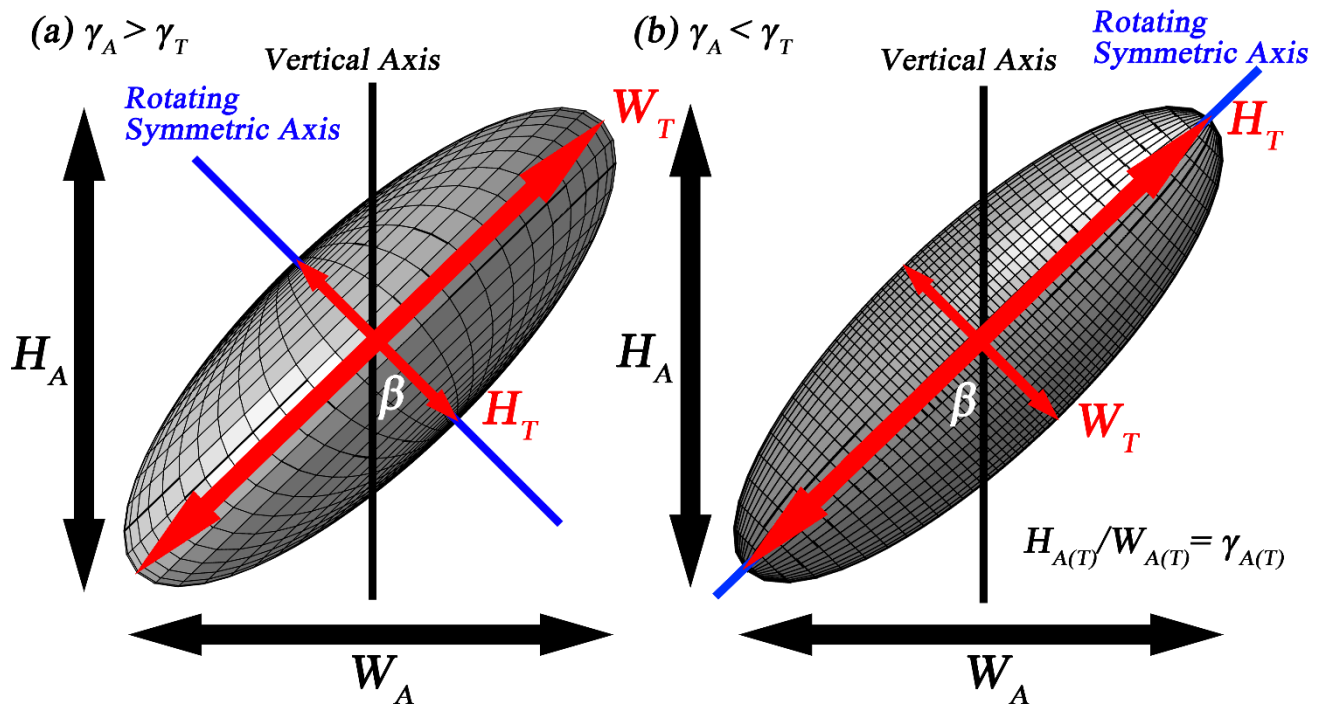
869

870   Figure 2. Conceptual model of an (a) oblate and (b) prolate spheroid with the same canting angle

871   (β). $W_{A(T)}$ and $H_{A(T)}$ are the apparent (true) width and height of the particle, respectively. $\gamma_{A(T)}$ is the

872   apparent (true) axis ratio.

873

874

875
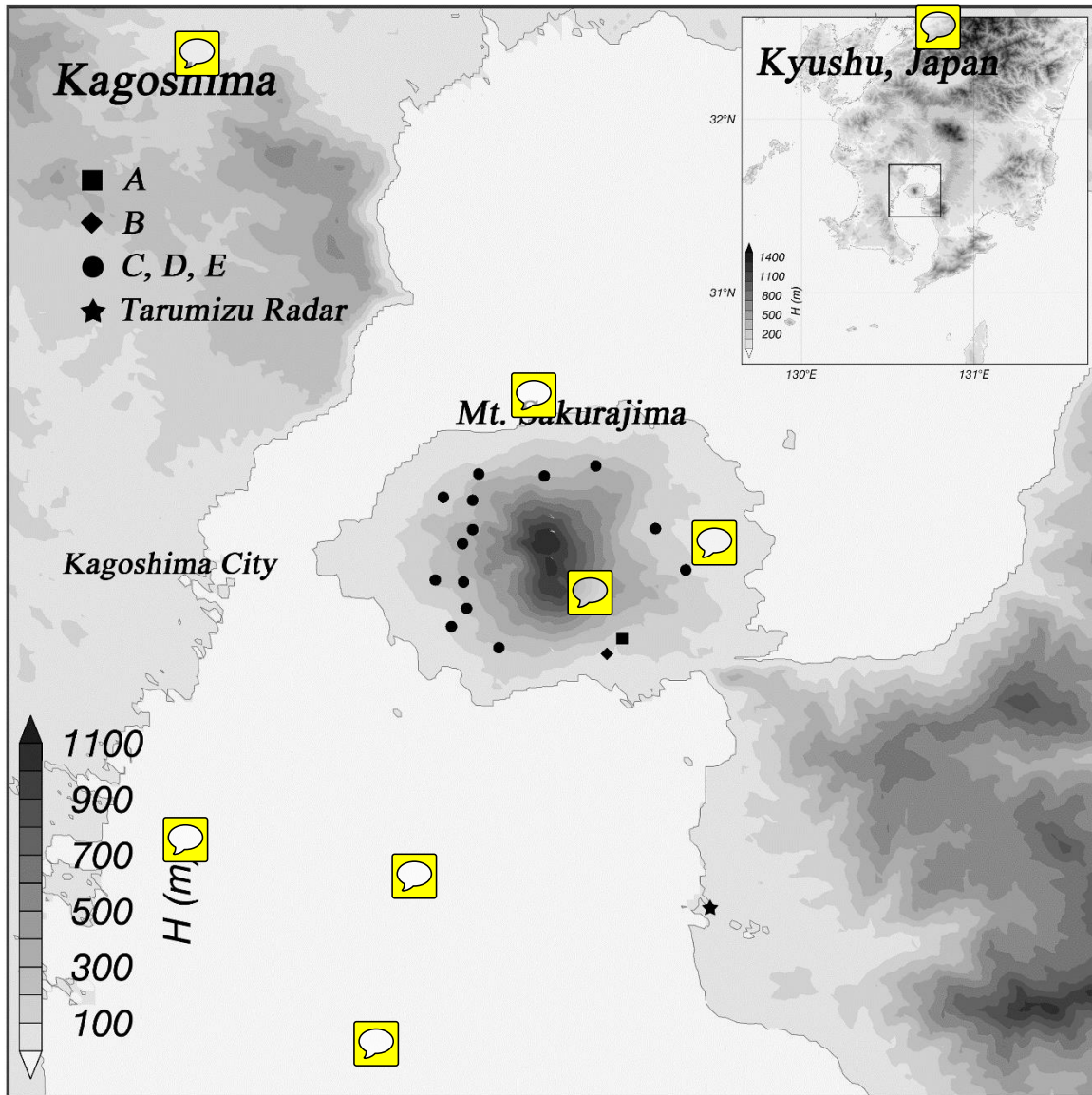
Figure 3. The locations of tephrometers and Showa crater on Sakurajima volcano, Japan. Black symbols indicate the locations of tephrometers and the star, square, and circle symbols correspond to datasets A, B and C–E, respectively. The white circle symbol represents the location of Showa crater.

883
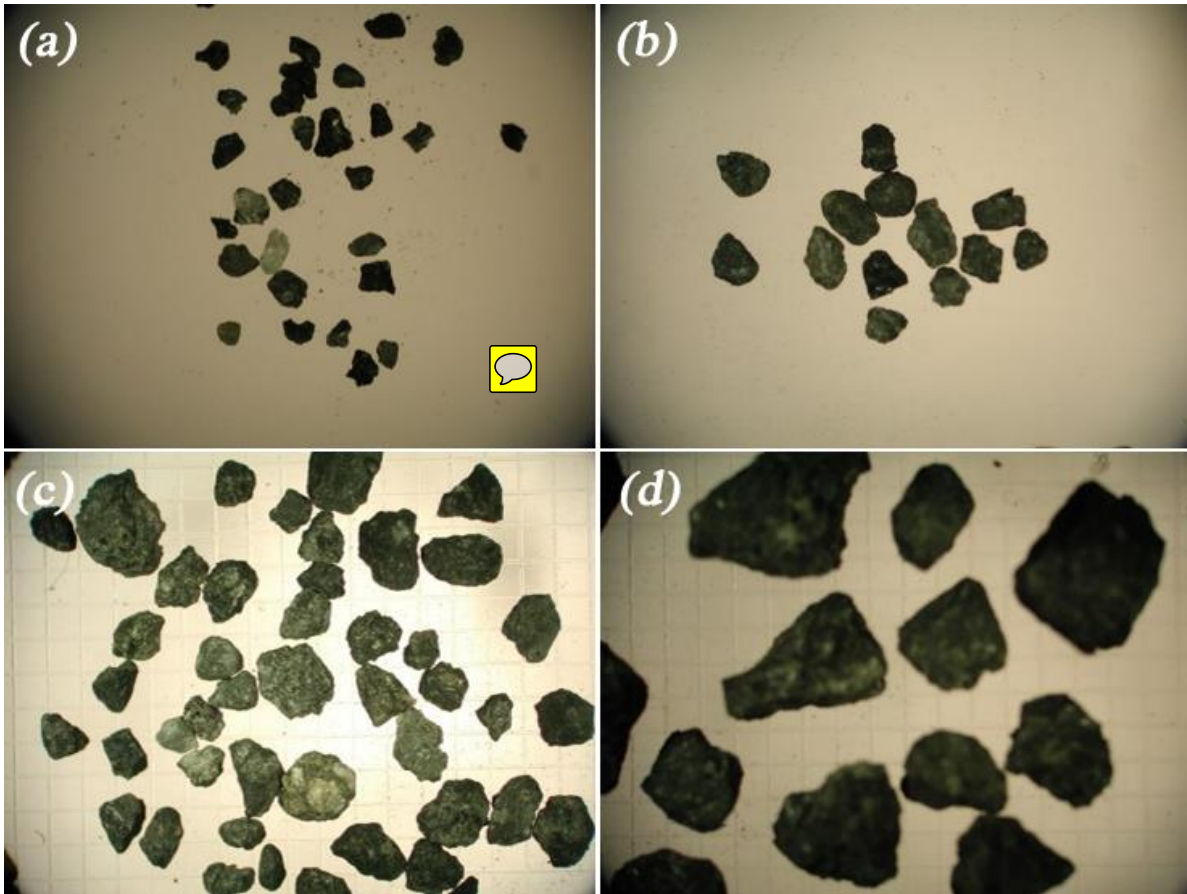
884 Figure 4. Real images of volcanic ash particles used in the present study. The particles were

885 classified as (a) 0.125 mm < D ≤ 0.25 mm, (b) 0.25 mm < D ≤ 1 mm, (c) 1 mm < D < 2 mm, and

886 (d) 2 < D ≤ 4 mm.

887

888

889
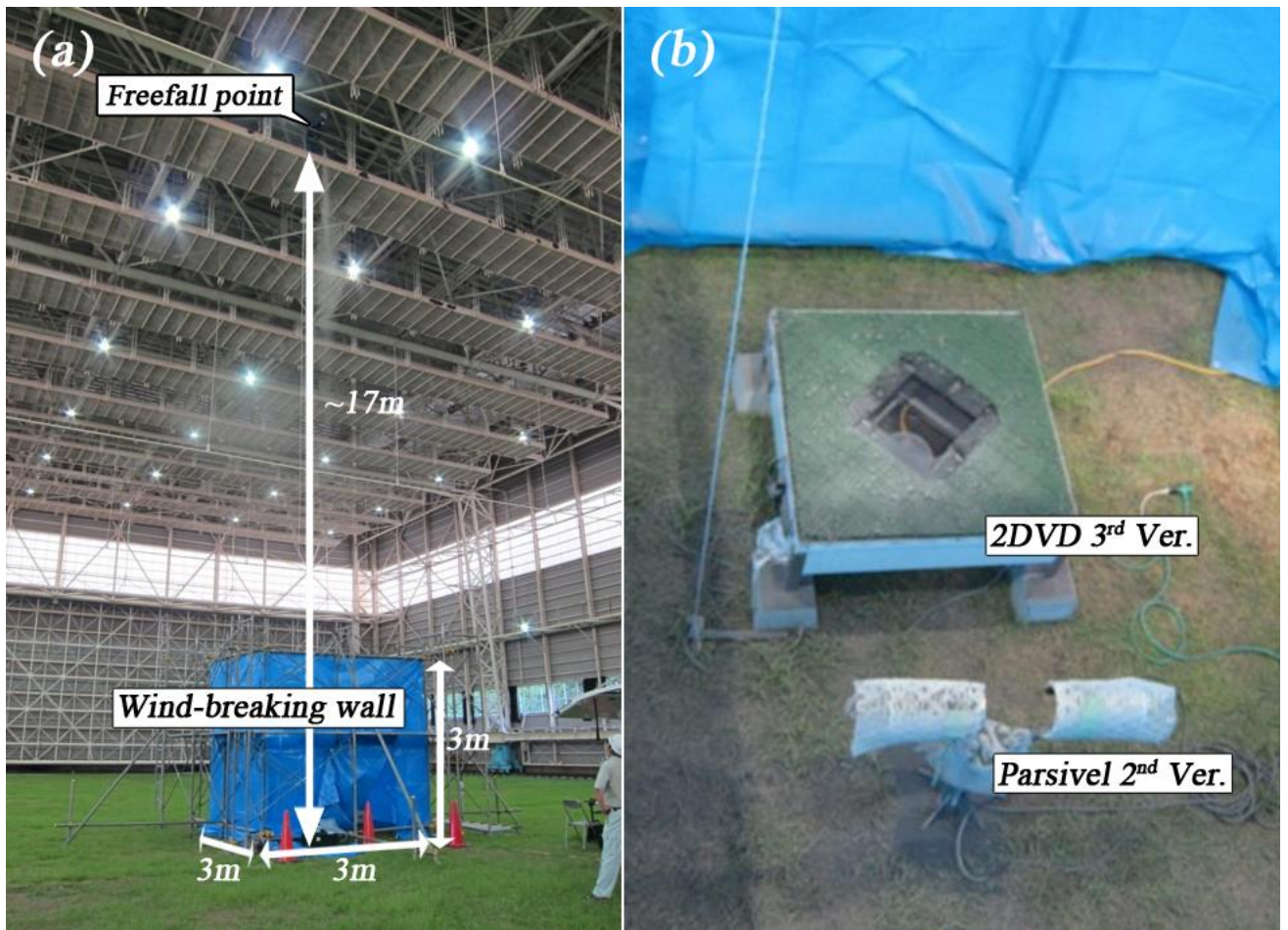
890
891 Figure 5. Free-fall experiment conditions of volcanic ash particles on the (a) outside and (b) inside
892 of the wind-breaking wall covering the disdrometers in the large-scale rainfall simulator of the National
893 Research Institute for Earth Science and Disaster Prevention (NIED).
894
895
896
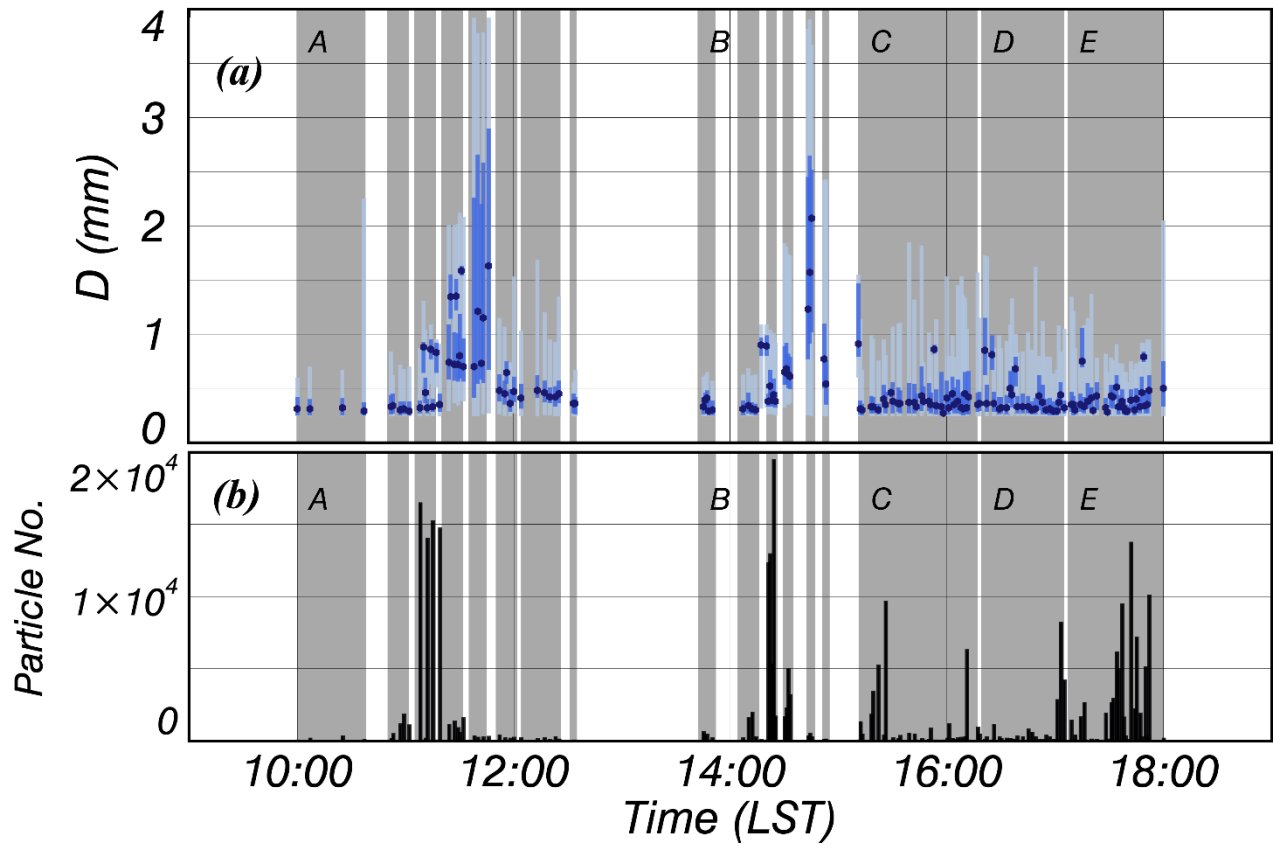
897

898   Figure 6. The 1-min interval time series of D and the number of particles in the free-fall

899   experiment conducted at the NIED.

900

901

902
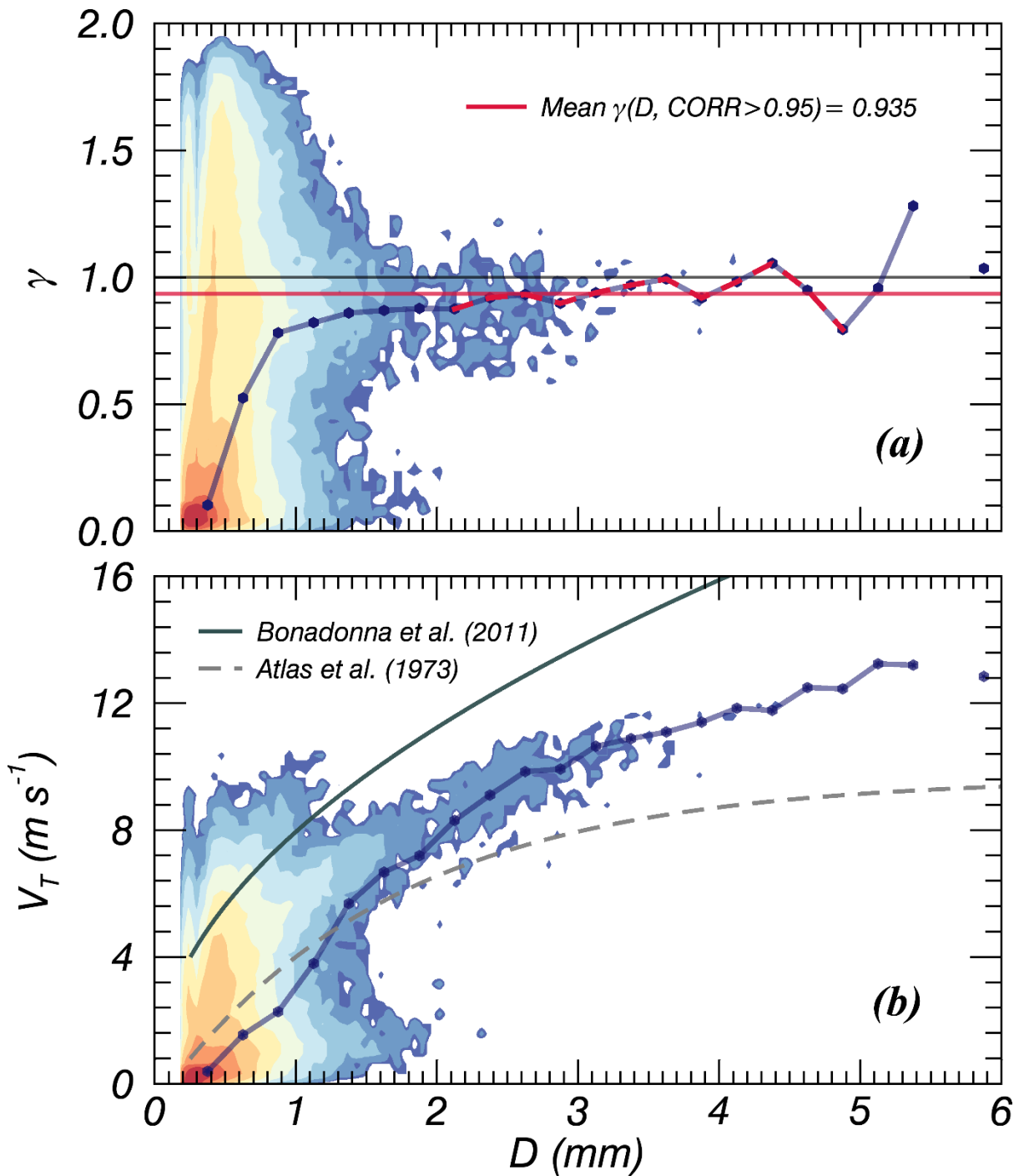
Figure 7. Contour image of volcanic ash particles for (b) the axis ratio (γ) and (b) terminal velocity (V$_T$) with respect to the raw data. Grey solid and broken lines are the relationships between volcanic ash particles and raindrops suggested by Bonadonna et al. (2011) and Atlas et al. (1971), respectively. The red solid line is the averaged γ satisfying the condition that the correlation coefficient exceeds 0.95.
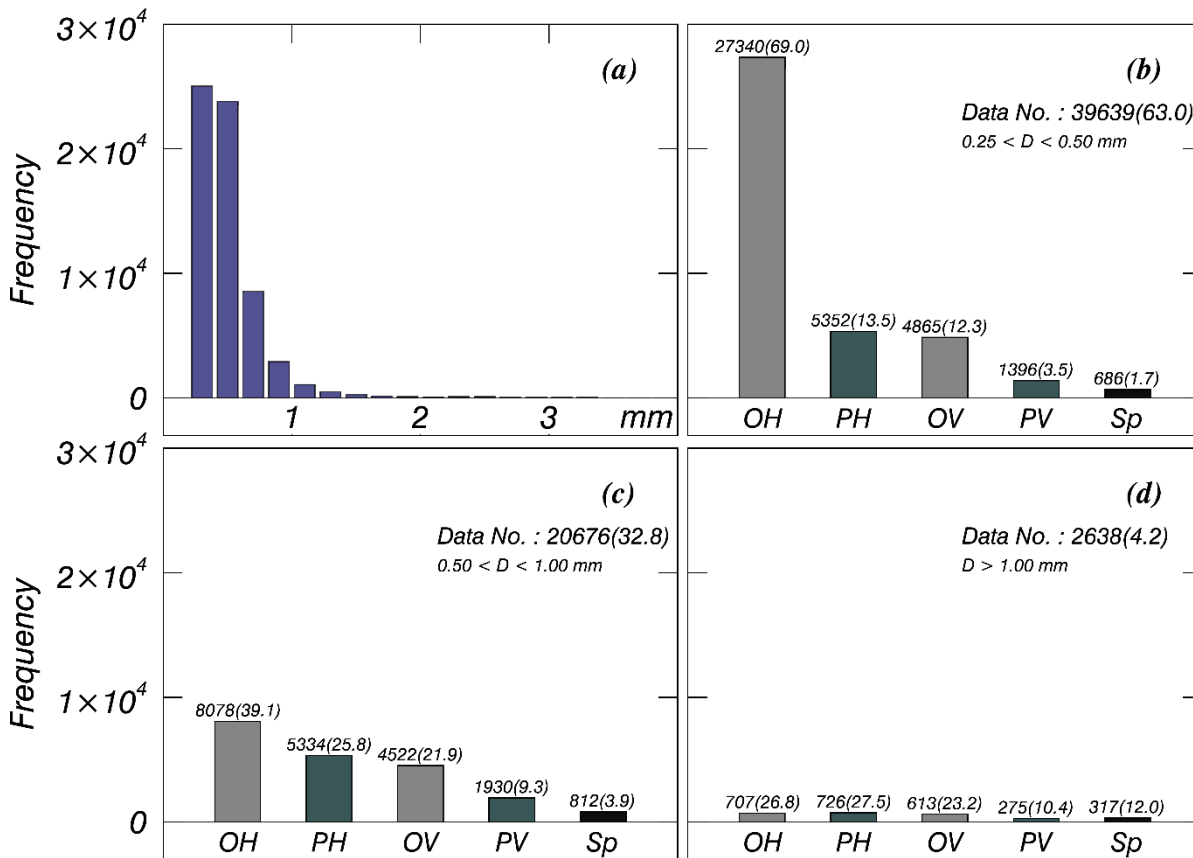
Figure 8. Histograms of volcanic ash particles for (a) all particle types and (b–d) each particle shape type of the phi scale. The grey- and dark grey-shaded (patterned) bars indicate horizontal oblate (OH) (vertical oblate [OV]) and horizontal prolate (PH) (vertical prolate [PV]), respectively. The black bar corresponds to spherical (Sp) particles. The number on the top of each bar plot is the number of data points and that in parenthesis is the percentage for each phi scale.
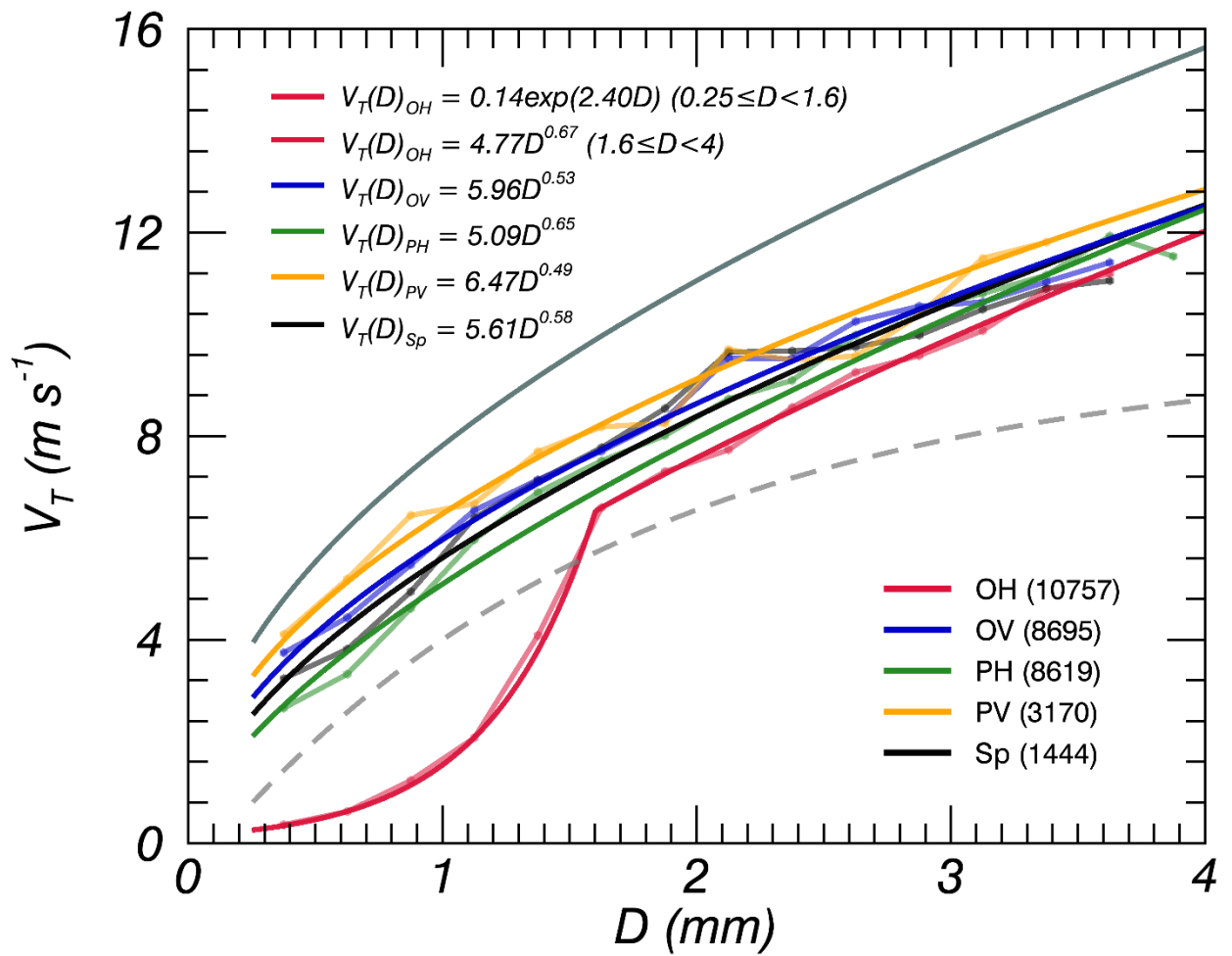
919

920   Figure 9. Distribution of median V_T values after applying a 60% V_T quality control (QC) threshold

921 for each particle shape type. The grey solid and broken lines show the relationships of volcanic ash

922 particles and raindrops suggested by Bonadonna et al. (2011) and Atlas et al. (1971), respectively.

923

924

925
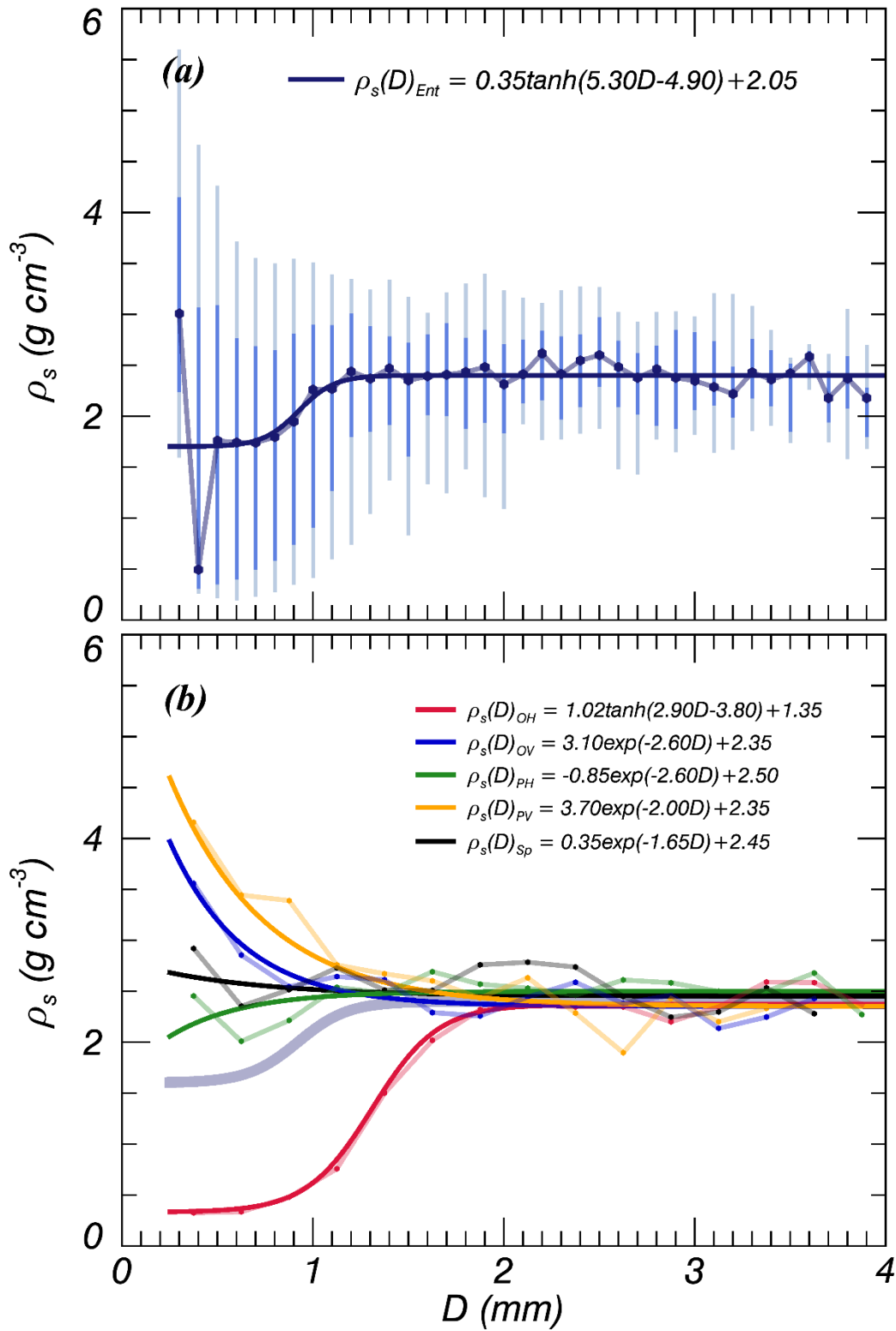
Figure 10. Distribution of (a) quartile and (b) median particle density (ρ_s) values after applying the 60% V_T QC threshold for all, and each individual, particle shape type, respectively.
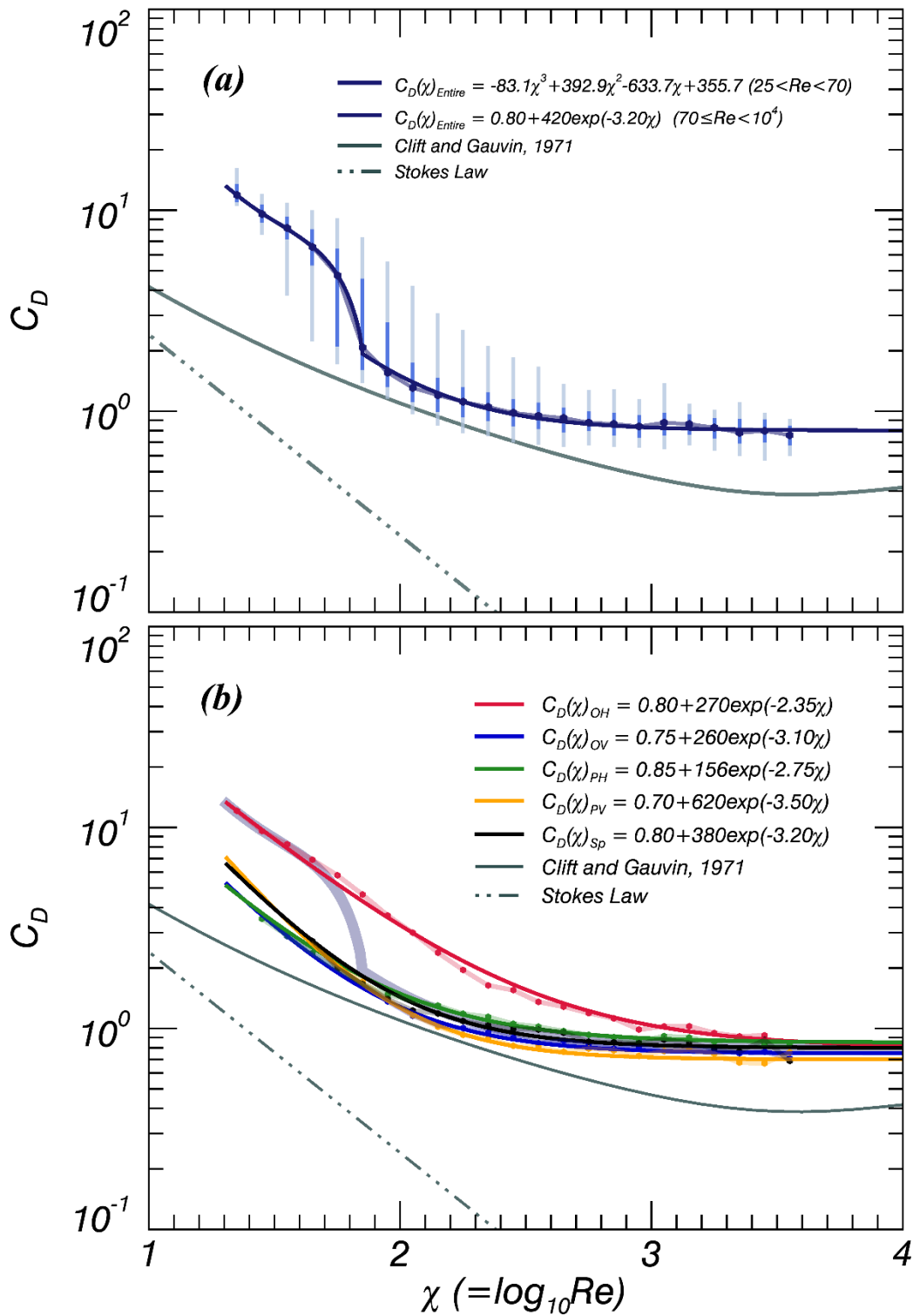
Figure 11. Same as Fig. 10 but for Reynolds number (Re) and drag coefficient (C_D). The grey solid and broken lines in (a) are the relationships of spheres suggested by Clift and Gauvin (1971) and Stokes (1851), respectively.

935
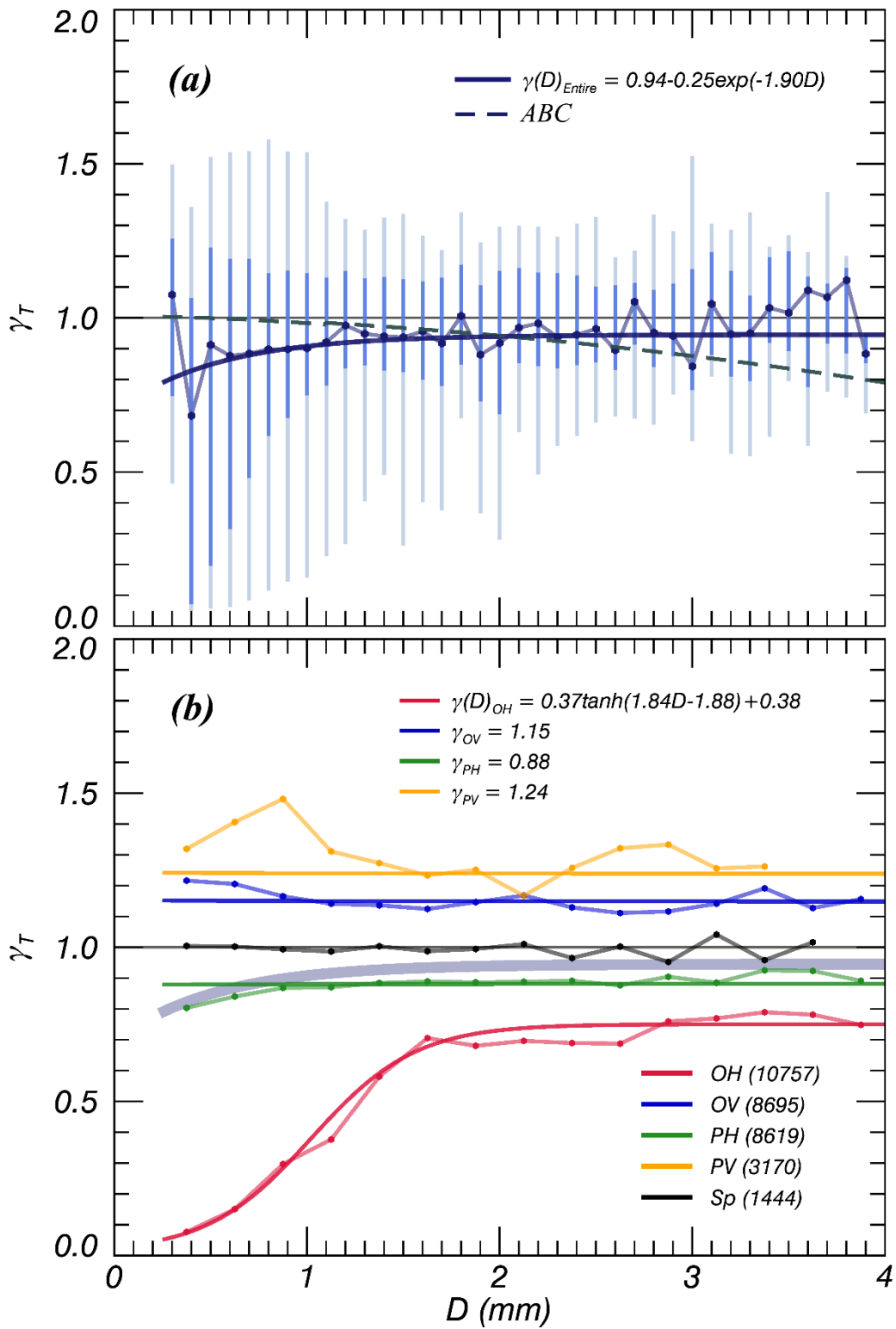
Figure 12. Same as Fig. 10 but for γ. The grey broken line (ABC) in (a) shows the relationships of

γ for raindrops suggested by Beard and Chuang (1987) and Andsager et al. (1999).
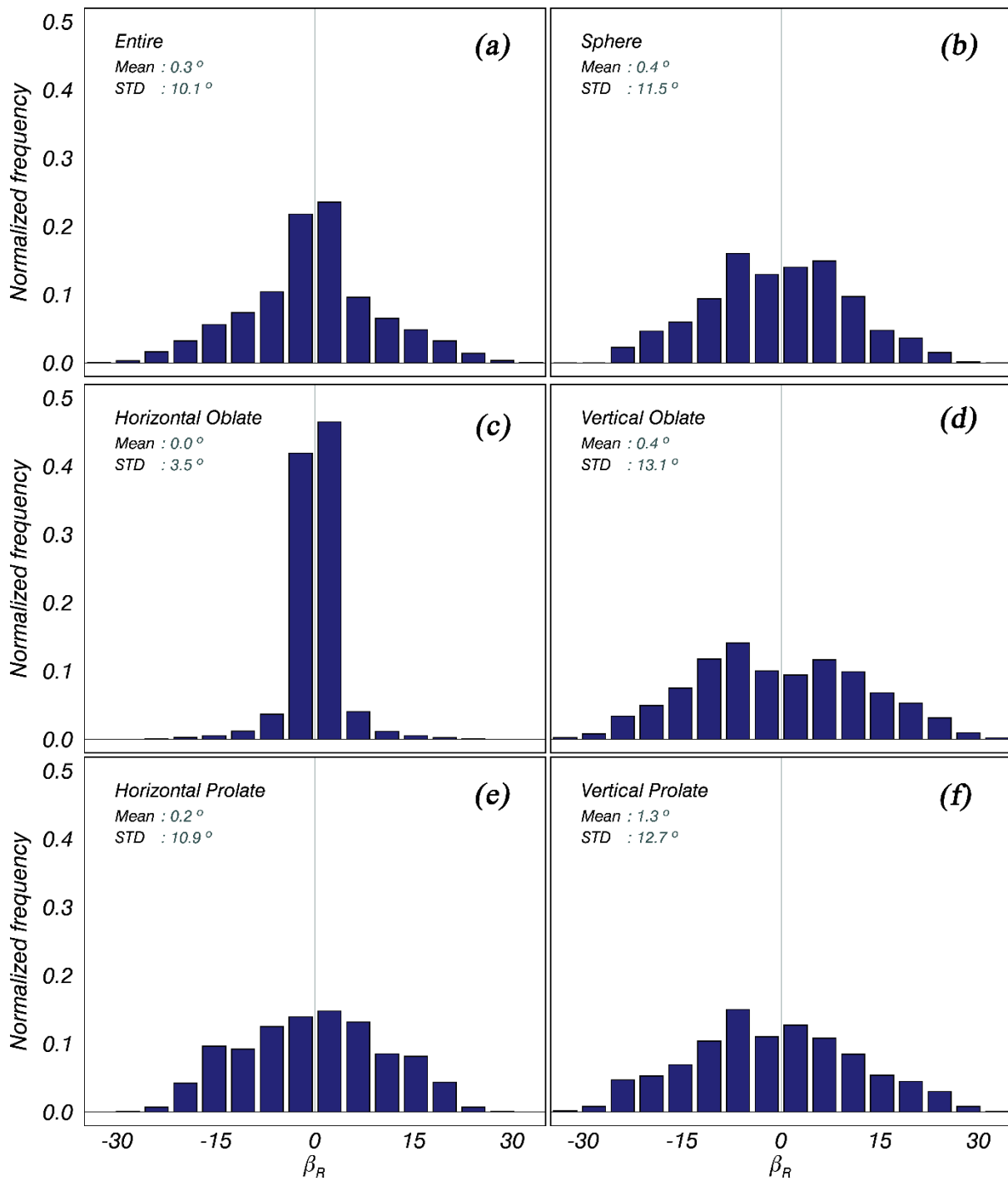
Figure 13. Histograms of representative canting angle (β_R) for each particle shape type, including the data for all particles.
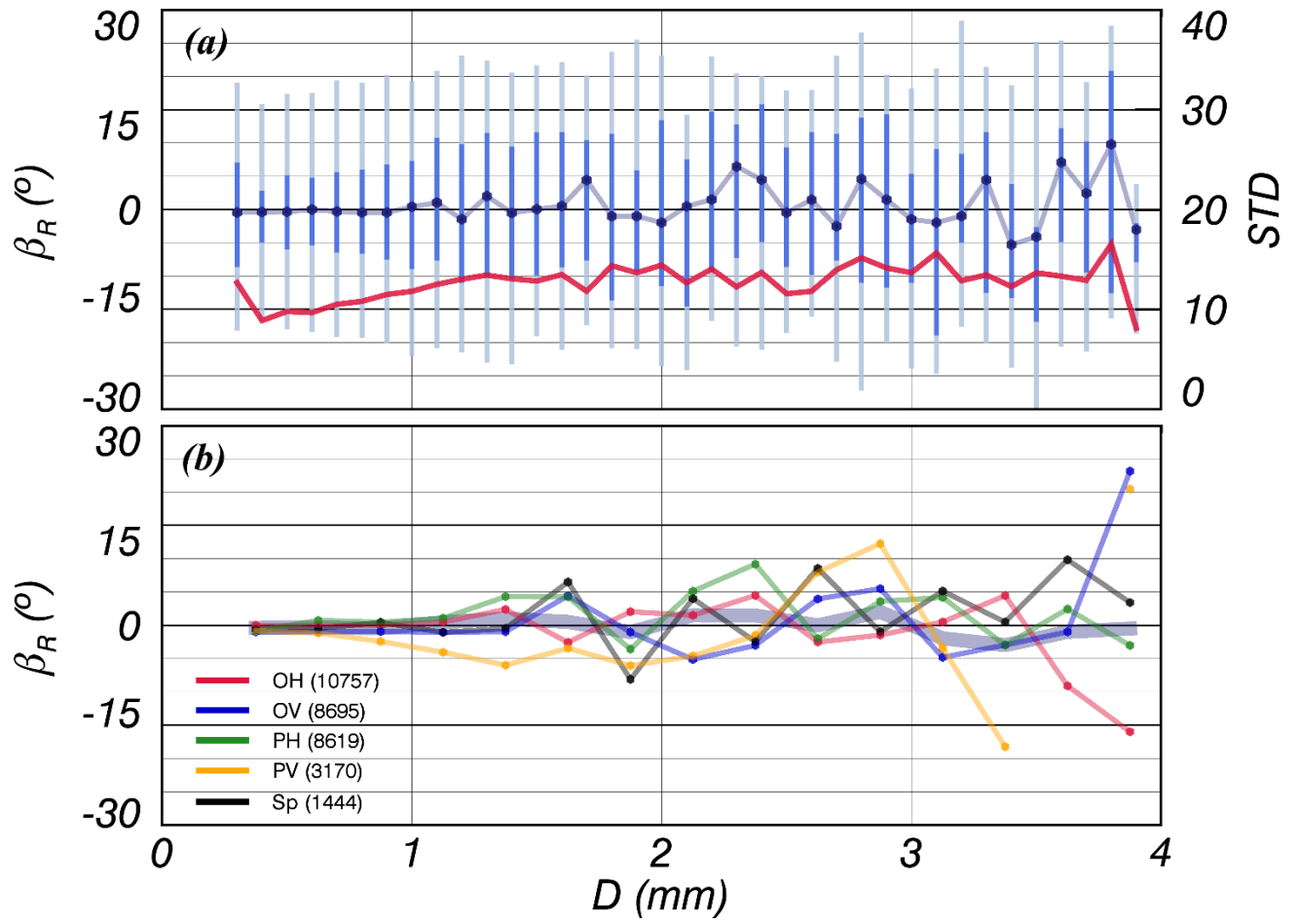
Figure 14. Distribution of β_R with D for each particle shape type including the data for all particles. The red solid line indicates the standard deviation.
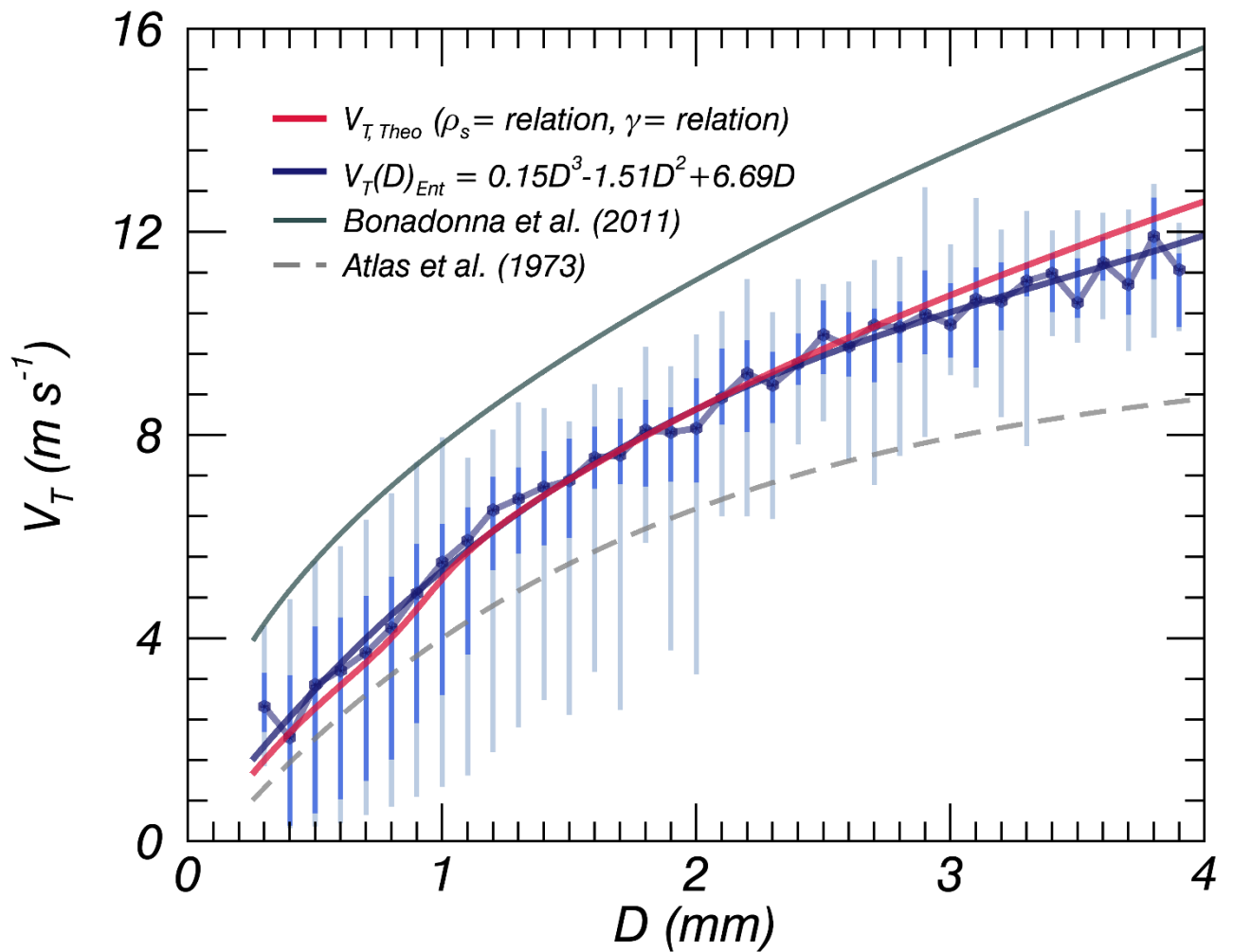
Figure 15. The V_T quartiles after applying the 60% V_T QC threshold for all, and each individual, particle shape type, respectively. Grey solid and broken lines in (a) are the relationships of volcanic ash particles and raindrops suggested by Bonadonna et al. (2011) and Atlas et al. (1971), respectively. The red solid line indicates the $V_{T,Ref}$ relationships of γ and particle density suggested by the present study.
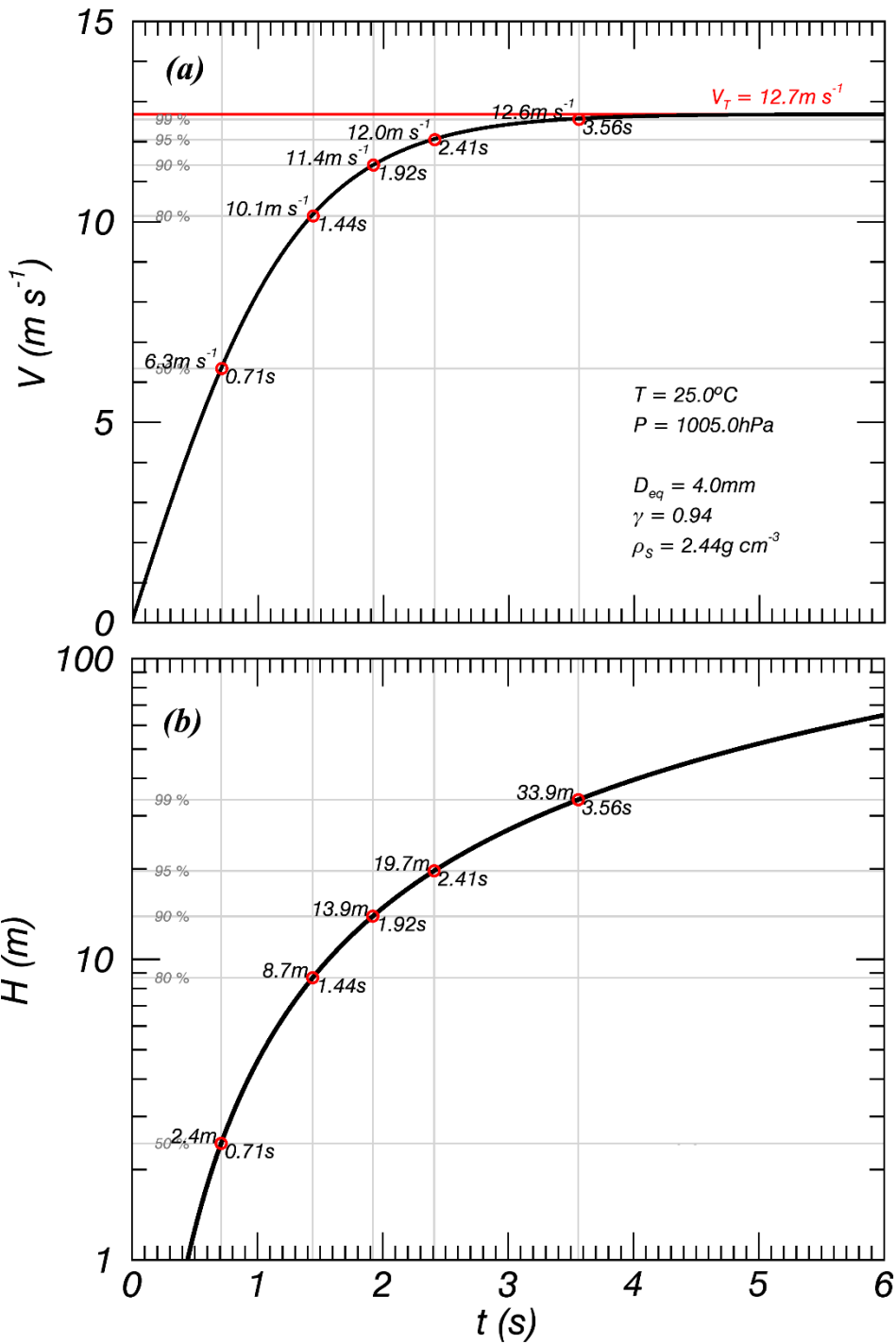
958

959   Figure A1. Theoretical (a) fall velocity and (b) falling height for a sphere with D = 4 mm,

960   considering the surface roughness coefficient of the volcanic ash particle (1.07[-1]) relative to its fall

961   velocity (Bagheri and Bonadonna, 2016).

962

Tables

Table 1. Particle number by particle shape type after applying quality controls and ash particle classification criteria.

Type	Description	Classification conditions	Data number (%)
All	All	.	62,953 (100)
OH	Horizontal oblate	$\gamma_{T1(2)} < 0.9$ $\|\gamma_{T1} - \gamma_{T2}\| \leq 0.1\gamma_T$	36,125 (57.38)
OV	Vertical oblate	$0.9 \leq \gamma_{T1(2)} \leq 1.1,$ $\gamma_{T2(1)} > 1.1$	10,000 (15.88)
PH	Horizontal prolate	$\|\gamma_{T1} - \gamma_{T2}\| > 0.1\gamma_T$	11,412 (18.13)
PV	Vertical prolate	$\gamma_{T1(2)} > 1.1$ $\|\gamma_{T1} - \gamma_{T2}\| \leq 0.1\gamma_T$	3,601 (5.72)
Sp	Sphere	$0.9 \leq \gamma_{T1(2)} \leq 1.1$ $\|\gamma_{T1} - \gamma_{T2}\| \leq 0.1\gamma_T$	1,815 (2.88)

968   Table 2. Information on the collected volcanic ash particles.

Data	Collection date	Re-analysis time (June 18, 2014)	Re-analysis method
A	Dec. 1–31 2008	10:00–12:34 (154 min)	Size by size (phi scale)
B	Mar. 1–31 2010	13:43–14:53 (70 min)	Size by size (phi scale)
C	Feb. 28, 2014	15:11–16:17 (66 min)	Mixed
D	Mar. 31, 2014	16:19–17:05 (46 min)	Mixed
E	Apr. 30 2014	17:07–18:00 (53 min)	Mixed

969

970

971   Table 3. Relationships of terminal velocity with the number of data points, the value of the

972   correlation coefficient (CC) and the root mean square error (RMSE) after applying the 60% V_T QC

973   threshold for each particle shape type.

Type	Data number (%)	Relationship (0.25 < D (mm) ≤ 4)	CC	RMSE
All	32685 (100)	$V_T(D) = 0.15D^3 - 1.51D^2 + 6.69D$	0.56	1.22
OH	10757 (34.12)	$V_T(D) = 0.14\exp(2.40D)\ (0.25 \le D < 1.6)$ $V_T(D) = 4.77D^{0.67}\ (1.6 \le D < 4)$	0.94	0.46
OV	8695 (26.60)	$V_T(D) = 5.96D^{0.53}$	0.75	0.85
PH	8619 (26.36)	$V_T(D) = 5.09D^{0.65}$	0.87	0.74
PV	3170 (9.69)	$V_T(D) = 6.47D^{0.49}$	0.71	0.96
Sp	1444 (4.41)	$V_T(D) = 5.61D^{0.56}$	0.91	0.78

974

975

976

977

978

979